Ocean Modelling 131 (2018) 115–131

Contents lists available at ScienceDirect

Ocean Modelling

journal homepage: www.elsevier.com/locate/ocemod

# Impact of the representation of the freshwater river input in the Western Mediterranean Sea

César Sauvage[*,a], Cindy Lebeaupin Brossier[a], Véronique Ducrocq[a], Marie-Noëlle Bouin[a,b], Béatrice Vincendon[a], Marco Verdecchia[c], Isabelle Taupier-Letage[d], Françoise Orain[e]

[a] CNRM, UMR 3589, Météo-France & CNRS, Toulouse, France
[b] CNRS, Ifremer, IRD, UBO / Laboratoire d'Océanographie Physique et Spatiale (LOPS), IUEM, Plouzané UMR 6523, France
[c] Department of Physical and Chemical Sciences, University of L'Aquila, L'Aquila, Italy
[d] Aix Marseille Univ., Université de Toulon, CNRS, IRD, MIO UM 110, Antenne de la Seyne, 83500, La Seyne, France
[e] Centre de Météorologie Spatiale, Météo-France, Lannion, France

ARTICLE INFO

*Keywords:*
Flood
Heavy precipitation
HyMeX
North-Western Mediterranean sea
River plumes
Runoff freshwater flux
Stratification

ABSTRACT

The Western Mediterranean Sea is often affected by heavy precipitation which frequently generates floods or even flash floods. These events generally produce brief but major freshwater inputs in the ocean. In order to evaluate the sensitivity to the representation of river freshwater input, three different runoff forcing dataset are used to drive the NEMO ocean model: a monthly climatology, an observational dataset with a daily or a hourly frequency. The sensitivity is investigated over the first Special Observation Period (SOP1) of the HyMeX program that took place in autumn 2012, in two configurations of NEMO: the first is WMED36 over the Western Mediterranean Sea at 1/36°-resolution and the second is a new configuration covering the North-Western Mediterranean Sea with a 1/72°-resolution named NWMED72. With NWMED72, the impact of the representation of the river freshwater flux, i.e. moving from a surface flux to a vertical distribution of the flux, is also evaluated. The results show that the ocean stratification is significantly modified locally in simulations where runoff observations are used compared to those using the climatology. The sea surface salinity is modified as well as the mixed layer which is thinner as bounded by a well marked halocline. The sea surface temperature is also impacted by the change in runoff frequency. Moreover, the current intensity in river plume during flood is increased. Vertical profiles of salinity and temperature and thus the mixed layer depth are changed when the runoff forcing is distributed over a depth. Those changes are limited and very local but the realism of the river runoff input is improved.

## 1. Introduction

The Mediterranean Sea is a semi-enclosed sea where all of the water exchanges are concentrated in the Strait of Gibraltar with the Atlantic Ocean and in the Bosphorus Strait with the Black Sea. Well-known as an evaporation basin, the loss of water in the atmosphere is compensated by an inflow of Atlantic water (AW) (Bormans et al., 1986; Mariotti et al., 2002), which circulates cyclonically at basin scale (see Millot and Taupier-Letage (2005) for a review). In the Western Basin it forms the eastward Algerian Current (AC, Fig. 1) and the southwestward Northern Current (NC, Fig. 1). The latter flows along slope from the Ligurian Sea to the Balearic Sea. The northern limit of the reservoir of AW is materialized by the North Balearic Front (NBF, Fig. 1). The associated eastward recirculation along the northern side of the NBF and the NC form a cyclonic gyre, interacting with atmosphere, continental surface and bathymetry (Fig. 1). During wintertime, the dry and cold regional winds (northerly Mistral and northwesterly Tramontane) can induce deep water formation in the Gulf of Lion, both by cascading and open-sea convection (Marshall and Schott, 1999; Houpert et al., 2016; Testor et al., 2018). During the stratified period, these winds induce upwelling cells in the Gulf of Lion (e.g. Millot (1990)) and frequent shallow anticyclonic eddies along its western coast (Rubio et al., 2009; Hu et al., 2011).

The Mediterranean Sea is also a region frequently affected by heavy precipitation events (HPEs). Such events are characterized by large amounts of accumulated rainfall in short time, typically more than 100 mm in 24h, associated with mesoscale convective systems (MCSs) (Ducrocq et al., 2016). Falling over small river catchments that are

* Corresponding author.
*E-mail address:* cesar.sauvage@meteo.fr (C. Sauvage).

https://doi.org/10.1016/j.ocemod.2018.09.005
Received 23 March 2018; Received in revised form 30 August 2018; Accepted 12 September 2018
Available online 18 September 2018
1463-5003/ 

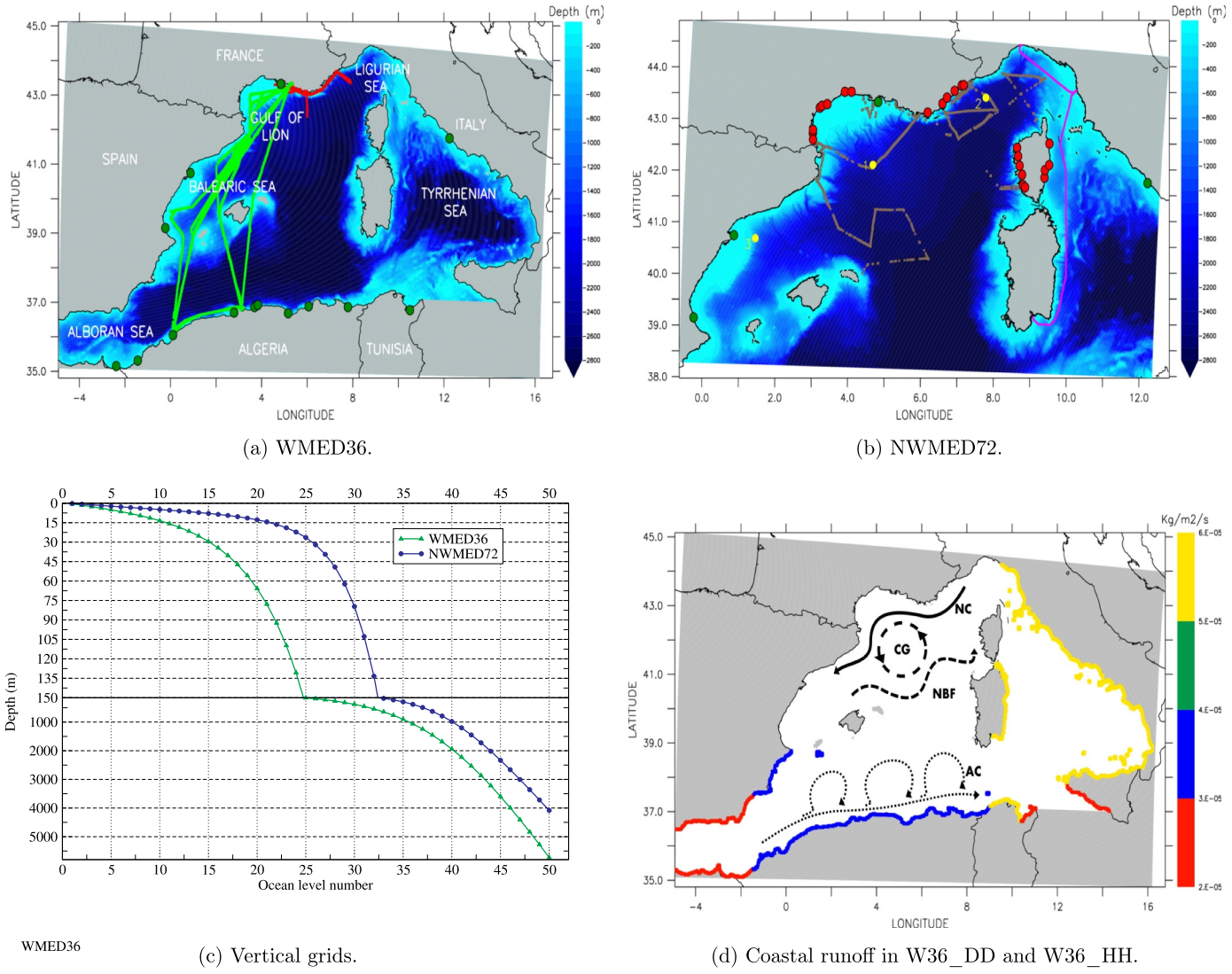


(a) WMED36.

(b) NWMED72.

(c) Vertical grids.

(d) Coastal runoff in W36_DD and W36_HH.

**Fig. 1.** Domains of the two ocean model configurations [bathymetry in meters]: (a) WMED36, (b) NWMED72 and (c) their vertical grids. (d) Coastal runoff (in kg/m$^2$/s) from climatology kept for W36_DD and W36_HH simulations. In (a,b): Green circles represent the main rivers in the climatology; Red circles represent rivers added with runoff observations; Coloured lines represent ship/TSG tracks: Marfret−Niolon in green, Téthys II in brown, Europe in red and Barcelona Express in purple; and yellow circles represent the moored buoys: 1 is GL, 2 is Az and 3 is Ta. In (d): NC is for Northern Current, NBF is for North Balearic Front, CG is for Cyclonic Gyre and AC is for Algerian Current. (For interpretation of the references to color in this figure legend, the reader is referred to the web version of this article.)

characteristic of the Mediterranean region (Tarolli et al., 2012; Merheb et al., 2016), these large and sudden precipitation amounts often lead to devastating flash floods and flooding events, causing damages and sometimes casualties (Buzzi et al., 1998; Romero et al., 1998; Krichak et al., 2004; Delrieu et al., 2005; Efstathiou et al., 2014; Ivančan-Picek et al., 2014)

HPEs and the associated flooding can produce large amount of freshwater input into ocean. Therefore, river freshwater runoff plays an important role on coastal regions. Freshwater flows from the river mouths to the ocean as a plume and previous studies have shown impact on the local circulation (e.g. Brando et al. (2015)). In most of the cases, water from the plume tends to flow along the coast with the land on the right in the northern hemisphere due to the influence of the Earth's rotation (Simpson, 1997). This low salinity buoyant freshwater alters stratification in the vicinity of the river mouth. Thus, a variability of the sea surface salinity (SSS) and the sea surface temperature (SST) is observed. Sometimes, it can be advected downstream and have an impact off-shore (Brando et al., 2015; Tseng et al., 2016; Fournier et al., 2016).

This study investigates the impact of a better representation of river runoffs in a high-resolution ocean model, with a focus in the Western Mediterranean area. Indeed, several case studies such as Schiller and Kourafalou (2010) and Herzfeld (2015) have shown that the way the river runoff is modeled impacts the river plume area and the mixing processes in coastal regions. More particularly a vertical distribution of the runoff flow can reduce low salinity surface bias (Tseng et al., 2016). The morphology of the plumes is sensitive to wind events and river discharges (Otero et al., 2008). More especially, in our area of interest, one of the largest rivers is the Rhône River, flowing in the Gulf of Lion with an average flow around 1 700 m$^3$/s. Its plume can extend far away (about 40 km) from the coast (Estournel et al., 1997) and presents a high variability depending on the meteorological conditions and outflow forcing (Broche et al., 1998; Estournel et al., 2001).

This study investigates how river plumes are represented and how a high temporal frequency flow can affect them, especially during floods. Moreover, we focus on how the heat and salt contents are impacted, along with the stratification, in the vicinity of river mouths. To evaluate the sensitivity to the representation of river runoff, the NEMO ocean

model is used, forced in surface by the atmospheric forecasts of the 2.5 km horizontal resolution AROME-WMED atmospheric model over a well-observed autumn period with the occurrence of several HPEs and river floods in the northwestern Mediterranean area. Two different ocean configurations are used (Fig. 1a and b), at a 1/36° and 1/72° horizontal resolutions. The sensitivity is investigated by comparison of ocean simulations, changing the river forcing in term of realism (climatology vs observations), frequency (monthly, daily, hourly) and distribution (surface input vs vertical distribution). First step is the validation of the two different configurations. Then the sensitivity to the frequency change of river runoff and to a more realistic vertical distribution of it, is evaluated using several diagnostics on SSS, SST and local circulation.

This paper is organized as follows: Section 2 presents a description of the ocean model used with two configurations, of the river runoff forcing dataset and of the ocean observations used for the validation. The latter is detailed in Section 3 while Section 4 presents results about the sensitivity to the different river runoff inputs. Conclusions and discussions are finally given in Section 5.

## 2. Context and model description

### 2.1. HyMeX Campaign

The Hydrological cycle in the Mediterranean Experiment (HyMeX) international programme (Drobinski et al., 2014) aims to investigate the hydrological cycle processes with emphasis on high-impact weather events over the Mediterranean region. Two fields campaigns were organized during fall 2012 and winter 2013 called Special Observation Period (SOP1 and SOP2 respectively). The SOP1 from 5 September to 6 November 2012 was particularly devoted to the documentation of heavy precipitation, with the deployment of more than 200 instruments on land as well as in the air and at sea (Ducrocq et al., 2014). In particular, several platforms monitoring the ocean surface and upper layer were deployed during the campaign. Most of these platforms were located in the north-western Mediterranean area and thus provide a valuable dataset to validate the ocean simulations.

### 2.2. Numerical set-up

#### 2.2.1. Configurations

The ocean model used is NEMO (version 3_6) (Madec and the NEMO Team, 2016) in two configurations. For these two configurations, the common physical parametrizations are the following. The Total Variance Dissipation (TVD) scheme is used for tracer advection in order to conserve energy and enstrophy (Barnier et al., 2006). The vertical diffusion follows the standard turbulent kinetic energy formulation of NEMO (Blanke and Delecluse, 1993). In case of unstable conditions, a higher diffusivity coefficient of 10 $m^2/s$ is applied (Lazar et al., 1999). The sea surface height is a prognostic variable solved thanks to the filtered free-surface scheme of Roullet and Madec (2000). A no-slip lateral boundary condition is applied and the bottom friction is parameterized by a quadratic function with a coefficient depending on the 2D mean tidal energy (Lyard et al., 2006; Beuvier et al., 2012). The diffusion is applied along isoneutral surfaces for the tracers using a laplacian operator with the horizontal eddy diffusivity value $\nu_h$. For the dynamics (velocity), a bi-Laplacian operator is used with the horizontal viscosity coefficient $\eta_h$.

The first configuration is the sub-regional eddy-resolving configuration covering the western Mediterranean basin (Fig. 1a), with a 1/36° horizontal resolution over an ORCA-grid (from 2 to 2.5 km resolution) named WMED36 (Lebeaupin Brossier et al., 2014). It uses 50 stretched z-levels in the vertical, with level thickness ranging from 1 m near the surface to 400 m at the sea bottom (i.e. around 4000 m-depth, Fig. 1c). The model has two radiative open boundaries: a west open-boundary at 4.8°W (nearly 60 km east of the Strait of Gibraltar) and a south open-boundary across the Sicily Channel (37°N). The Strait of Messina between Sicily and continental Italy is closed. In WMED36, $\nu_h$ is fixed at 30 $m^2/s$ and $\eta_h$ at -1.$10^9$ $m^4/s$.

The second configuration covers the northwestern Mediterranean basin (Fig. 1b), with a 1/72° horizontal resolution (from 1 to 1.3 km resolution) and is called NWMED72. For this one, a new bathymetry was built from the interpolation of a 1/120° horizontal resolution topography with a particular attention on the islands, coastlines and river mouths. 50 stretched z-levels are also used in the vertical but with a higher refinement near the surface and thus a first level thickness of 0.5 m (Fig. 1c). This configuration has 2 two open boundaries: a south open-boundary near 38°N south of the Balearic Islands and Sardinia, and a east open-boundary across the Tyrrhenian Sea (12.5°E). In NWMED72, $\nu_h$ is fixed at 15 $m^2/s$ and $\eta_h$ is fixed at $-$ 1. $10^8$ $m^4/s$.

#### 2.2.2. Model forcing and initial conditions

Every simulation begins on 1 September 2012 until the 4 November 2012. In the following, this simulation period will sometimes be called SOP1 for simplification. Simulations are driven at the air-sea interface by the heat (the short-wave radiation minus the long-wave radiation minus the sensible and latent heat fluxes), freshwater (evaporation minus precipitation) and momentum fluxes taken from the AROME-WMED forecast (Fourrié et al. (2015), *doi:10.6096/HYMEX.AROME_WMED.2012.02.20*). This atmospheric forcing dataset was already used in Lebeaupin Brossier et al. (2014) and Léger et al. (2016) as it well reproduces, with a high resolution (2.5 km) and frequency (1h), the SOP1 meteorological conditions.

The initial conditions on the 1 September 2012 for the conservative temperature ($\theta$) and absolute salinity (S) are provided by the Mercator Océan daily PSY2V4R4 analysis (1/12° horizontal resolution) (Lellouche et al., 2013). Ocean velocity is initially null. The open-boundary conditions ($\theta$, S and velocities U,V) are also provided by the PSY2V4R4 mean fields at a monthly frequency for WMED36 (as in Lebeaupin Brossier et al. (2014)) and at a daily frequency for NWMED72.

#### 2.2.3. River runoff data set

All the rivers used in the simulations are described in Fig. 1a, b and Table 1. In NWMED72, a total of 28 rivers are considered whereas 38 rivers are considered in WMED36. In this study, we collected river flow observations to increase the accuracy of the freshwater input. This is done for the 28 rivers in NWMED72 domain. Daily and hourly observations for french rivers were collected from the french institute "Banque Hydro". Spanish and Italian main rivers observations were provided by the Ministerio de Agricultura, Alimentación y Medio Ambiente and by the University of L'Aquila, respectively. For the Ebro and Jucar Rivers only daily observations were available. The hourly set is then built from the daily set and consists in 24 consecutive identical values (Fig. 2b and c). For the Tibre, only hourly observations were available. So, the daily runoff is built from the average of the hourly set (Fig. 2a). For each river, runoff observations are taken at the hydrological station the nearest from the river mouth.

The runoff monthly climatology from Beuvier et al. (2010) is also used. This climatology was built using the climatological average of Ludwig et al. (2009) dataset to compute monthly runoff values. It is based on the values of 33 main rivers on the whole Mediterranean sea, listed in the RivDis database (Vörösmarty et al., 1996). Furthermore, in this climatology all the runoff of the secondary rivers are gathered and averaged by subbasin described in Ludwig et al. (2009) and put as a coastal runoff uniformly distributed over the coastal grid points.

Fig. 2 represents all the runoff time-series available for 4 main rivers in the northwestern Mediterranean during the SOP1. There is a significant difference between observations and climatological data set. Indeed, on Fig. 2d, which represents the Rhône River, the peak flow of the Intense Observation Period (IOP) 7a at the end of September and IOP13 occurring mid October appear clearly with the observations

**Table 1**
River mouth location; in italic font the rivers present in the climatology; underlined the rivers only present in WMED36; "OBS" stands for "available in observed data"; "Clim" for "contained in the Ludwig et al. (2009)'s climatology".

| River | Longitude | Latitude | Source | River | Longitude | Latitude | Source |
|---|---|---|---|---|---|---|---|
| Var | 7.1°E | 43.7°N | OBS | Gravone | 8.8°E | 41.9°N | OBS |
| Loup | 7.1°E | 43.7°N | OBS | Porto | 8.7°E | 42.3°N | OBS |
| Siagne | 6.9°E | 43.6°N | OBS | Liamone | 8.7°E | 42.1°N | OBS |
| Argens | 6.7°E | 43.4°N | OBS | Taravo | 8.8°E | 41.7°N | OBS |
| Giscle | 6.7°E | 43.2°N | OBS | Rizzanese | 8.8°E | 41.7°N | OBS |
| Gapeau | 6.2°E | 43.1°N | OBS | *Ebro* | 0.8°W | 40.8°N | OBS / Clim |
| *Rhône* | 4.8°E | 43.5°N | OBS / Clim | *Jucar* | 0.2°W | 39.2°N | OBS / Clim |
| Vidourle | 4.1°E | 43.5°N | OBS | *Tibre* | 12.2°E | 41.7°N | OBS / Clim |
| Lez | 3.9°E | 43.5°N | OBS | *Moulouya* | 2.4°W | 35.2°N | Clim |
| Herault | 3.4°E | 43.3°N | OBS | *Tafna* | 1.4°W | 35.3°N | Clim |
| Orb | 3.3°E | 43.3°N | OBS | *Cheliff* | 0.1°E | 36.1°N | Clim |
| Aude | 3.2°E | 43.2°N | OBS | *Mazafran* | 2.8°E | 36.7°N | Clim |
| Agly | 3.0°E | 42.8°N | OBS | *Isser* | 3.7°E | 36.9°N | Clim |
| Têt | 3.0°E | 42.7°N | OBS | *Sebaou* | 3.8°E | 36.9°N | Clim |
| Tech | 3.0°E | 42.6°N | OBS | *Soumman* | 5.1°E | 36.7°N | Clim |
| Golo | 9.5°E | 42.5°N | OBS | *El Kebir* | 6.0°E | 36.9°N | Clim |
| Tavignano | 9.5°E | 42.1°N | OBS | *Seybouse* | 7.8°E | 36.9°N | Clim |
| Fium-Orbo | 9.4°E | 42°N | OBS | *Mejerdah* | 10.6°E | 36.8°N | Clim |
| Solenzara | 9.4°E | 41.9°N | OBS | | | | |
| Fango | 8.7°E | 42.4°N | OBS | | | | |

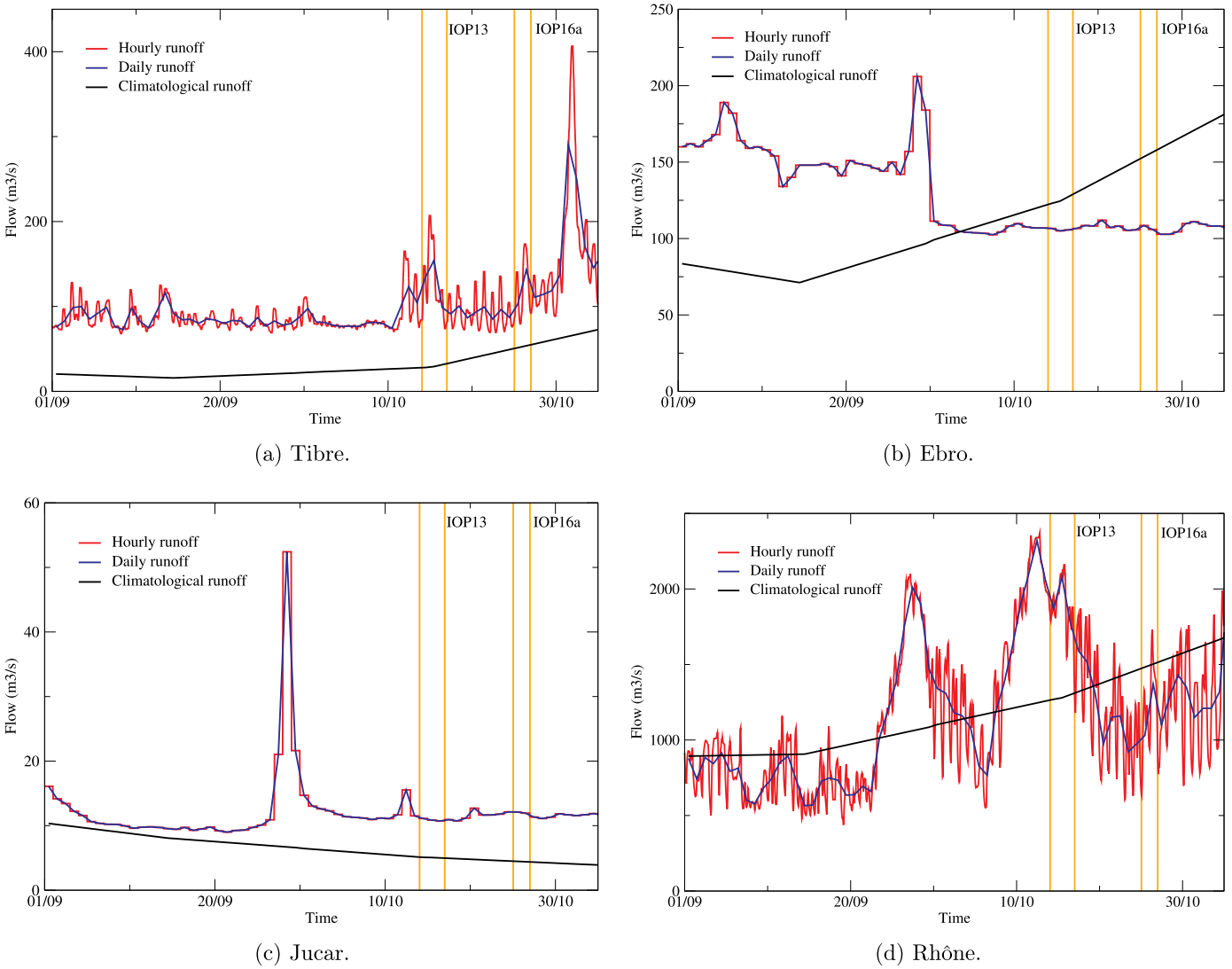


**Fig. 2.** Runoff ($m^3/s$) time-series during the SOP1 for (a) Tibre, (b) Ebro, (c) Jucar and (d) Rhône rivers: in black from the Ludwig et al. (2009) climatology, in blue from the daily data set and in red from the hourly data set. Orange lines mark IOP13 and 16a [see details in Ducrocq et al. (2016)]. (For interpretation of the references to color in this figure legend, the reader is referred to the web version of this article.)

**Table 2**
Scores (bias in °C, RMSE in °C, correlation) for SST compared to the three moored buoys (GL, Az, Ta), the Marfret-Niolon Thermosalinograph (MN), the Téthys II TSG (TY) and the Europe and the Barcelona Express TSGs (Eu, Ba).

| | GL | | | Az | | | Ta | | |
|---|---|---|---|---|---|---|---|---|---|
| | Bias | RMSE | Corr. | Bias | RMSE | Corr. | Bias | RMSE | Corr. |
| W36_CL | -0.37 | 0.83 | 0.92 | 1.36 | 1.68 | 0.86 | -0.20 | 0.60 | 0.96 |
| W36_DD | -0.37 | 0.83 | 0.92 | 1.36 | 1.68 | 0.86 | -0.19 | 0.59 | 0.96 |
| W36_HH | -0.37 | 0.83 | 0.92 | 1.35 | 1.68 | 0.86 | -0.19 | 0.59 | 0.96 |
| N72_CL | -0.40 | 0.84 | 0.92 | 1.06 | 1.33 | 0.92 | 0.38 | 0.75 | 0.94 |
| N72_DD | -0.31 | 0.90 | 0.89 | 1.06 | 1.34 | 0.92 | 0.37 | 0.75 | 0.94 |
| N72_HH | -0.27 | 0.92 | 0.88 | 1.06 | 1.34 | 0.92 | 0.37 | 0.74 | 0.94 |
| N72_DD_z | -0.30 | 0.90 | 0.88 | 1.07 | 1.34 | 0.92 | 0.38 | 0.75 | 0.94 |
| | MN | | | TY | | | EuBa | | |
| | Bias | RMSE | Corr. | Bias | RMSE | Corr. | Bias | RMSE | Corr. |
| W36_CL | 0.71 | 1.43 | 0.89 | 0.73 | 1.44 | 0.74 | 1.93 | 2.14 | 0.76 |
| W36_DD | 0.71 | 1.43 | 0.89 | 0.73 | 1.44 | 0.74 | 1.93 | 2.14 | 0.76 |
| W36_HH | 0.71 | 1.42 | 0.89 | 0.73 | 1.44 | 0.74 | 1.93 | 2.14 | 0.76 |
| N72_CL | 0.47 | 1.3 | 0.89 | 0.77 | 1.34 | 0.82 | 1.37 | 1.85 | 0.71 |
| N72_DD | 0.46 | 1.31 | 0.89 | 0.49 | 1.31 | 0.76 | -0.12 | 3.39 | 0.59 |
| N72_HH | 0.46 | 1.31 | 0.89 | 0.76 | 1.34 | 0.82 | 0.66 | 2.80 | 0.58 |
| N72_DD_z | 0.45 | 1.30 | 0.89 | 0.76 | 1.34 | 0.82 | -0.25 | 0.62 | 0.99 |

whereas they are obviously absent in the monthly climatology. In the following, the freshwater budget is calculated considering the WMED36 domain over the whole period of the simulation. For the climatological runoff dataset it is about 2477 $m^3/s$ included 1126 $m^3/s$ of coastal runoff which represents almost 50% of the total, whereas the contribution of freshwater for the daily runoff dataset is about 2142 $m^3/s$ with 482 $m^3/s$ for the coastal runoff. The contribution for the hourly runoff dataset is nearly the same as for the daily runoff dataset with 2137 $m^3/s$ of total freshwater with 482 $m^3/s$ of coastal runoff. The total amount of freshwater is larger in the climatological dataset due to the coastal runoff added along the coasts to figure all the secondary rivers. When only considering the main rivers, they have indeed a larger contribution in the daily and hourly observations than in climatology, as shown in Fig. 2. In summary, this means that the secondary rivers, which are now explicitly included, bring less water than the climatological coastal runoff. This, knowing that several rivers are missing in the observational datasets (notably outside France) but that there are also large uncertainties in the climatological coastal runoff values. The daily and hourly observations improves the realism of the river forcing with a greater spatial and temporal variability. It can also be noticed that a sub-daily variation of the runoff is observed on Fig. 2a and d.

Consequently, three types of river runoff forcing are applied. In WMED36 the first simulation named W36_CL uses the climatological data and coastal runoff on the whole domain. The second one uses daily observations (Table 1) where available and climatological data over the south and west subbasins (see, Fig. 1d) and is called hereafter W36_DD. The last one is the same but with hourly observations and is named W36_HH. In W36_DD and W36_HH the coastal runoff is as displayed in the Fig. 1d. Indeed, a part of the coastal runoff is deleted where new river runoffs observation are added. In NWMED72 the coastal runoff is never used in order to consider more realistic simulations. The first river forcing uses climatological data of the 4 majors rivers (Rhône, Tibre, Ebro and Jucar), called N72_CL, the second one uses daily runoff observations, called N72_DD, and the last one hourly runoff observations, named N72_HH.

For each configuration, river mouths are located in the domain using the nearest grid-point from their exact locations. In all the simulations described before, the river inflow is injected at the surface as if it was precipitation. The version 3_6 of NEMO allows us to change the way the river input is applied with the possibility to prescribe it over a defined depth rather than only at the surface. This method is only used here with NWMED72. This last simulation called N72_DD_z has the same characteristics as the one with daily river runoff but the inflow is distributed over several ocean levels (see Section 4).

## 3. Validation

In this section, the validation is done by comparison of the simulations against several ocean surface observations using data from moored buoys, ships and satellites. For all of them, only values with the highest quality index are kept for validation.

The observed dataset is inhomogeneous in space and time (see Fig. S1 and - Table S1 in the supplement). The simulated SSS (Sea Surface practical Salinity) and SST (Sea Surface potential Temperature) were extracted from the model at the nearest grid point of the ocean observation locations. The closest output in time is also chosen, knowing that, WMED36 outputs are given every 3 hours whereas NWMED72 has hourly outputs for ocean surface fields. For each observed dataset, a comparison is done via several scores such as the bias (model minus observation), the root mean square error (RMSE) and the correlation coefficient over the simulation period, from the 1 September to the 4 November. Although all the simulations have been compared to observations, this section mainly presents the results of W36_CL and N72_CL for more clarity. This also permits to complement the validation works of Lebeaupin Brossier et al. (2014) and Léger et al. (2016) that used the WMED36 configuration with the climatological runoff forcing.

First, moored buoys give the observed series of atmospheric parameters (2 m-temperature, 2 m-humidity, 10 m-wind speed, direction and gust intensity, mean sea level pressure), wave parameters (height and period), as well as ocean parameters (SST and SSS). The SST and SSS observations of three buoys are used in this study (see Fig. 1b), the Lion buoy (hereafter GL, located at 4.7°E-42.1°N) and the Azur buoy (hereafter Az, at 7.8°E-43.4°N) of Météo-France, and, the Tarragona buoy (hereafter Ta at 1.5°E–40.7°N) of Puertos del Estado. Tables 2 and 3 summarize the scores against buoys. In W36_CL, the SST is in good agreement with the GL and Ta buoys with a negative bias of less than 0.4 °C and a correlation coefficient above 0.9 (Fig. 3d and f). For the Az buoy, the bias is higher due to an overestimation in late October (Fig. 3b) that is explained by a transport of warmer water by the NC. Still, a good correlation coefficient is obtained over the period (Table 2). In N72_CL, the bias is reduced at the Az buoy with an improvement of the correlation coefficient. Yet an overestimation is

**Table 3**
As Table 2 but for SSS, bias and RMSE in psu.

| | GL | | | Az | | | Ta | | |
|---|---|---|---|---|---|---|---|---|---|
| | Bias | RMSE | Corr. | Bias | RMSE | Corr. | Bias | RMSE | Corr. |
| W36_CL | −0.14 | 0.16 | 0.14 | −0.25 | 0.27 | 0.08 | -0.48 | 0.55 | 0.18 |
| W36_DD | −0.14 | 0.16 | 0.14 | −0.25 | 0.26 | 0.07 | −0.49 | 0.55 | 0.21 |
| W36_HH | −0.14 | 0.16 | 0.14 | −0.25 | 0.26 | 0.06 | −0.49 | 0.55 | 0.21 |
| N72_CL | −0.15 | 0.18 | 0.33 | −0.25 | 0.26 | 0.24 | −0.52 | 0.56 | 0.28 |
| N72_DD | −0.16 | 0.19 | 0.39 | −0.25 | 0.27 | 0.24 | −0.51 | 0.55 | 0.24 |
| N72_HH | −0.16 | 0.19 | 0.41 | −0.25 | 0.27 | 0.24 | −0.51 | 0.55 | 0.23 |
| N72_DD_z | −0.16 | 0.19 | 0.42 | −0.25 | 0.27 | 0.24 | −0.51 | 0.55 | 0.22 |
| | MN | | | TY | | | EuBa | | |
| | Bias | RMSE | Corr. | Bias | RMSE | Corr. | Bias | RMSE | Corr. |
| W36_CL | −0.30 | 0.48 | 0.67 | −0.22 | 0.40 | 0.02 | 0.51 | 2.44 | 0.63 |
| W36_DD | −0.30 | 0.49 | 0.67 | −0.22 | 0.40 | −0.01 | 0.48 | 2.44 | 0.63 |
| W36_HH | −0.30 | 0.49 | 0.67 | −0.22 | 0.40 | −0.01 | 0.48 | 2.44 | 0.63 |
| N72_CL | −0.28 | 0.48 | 0.53 | −0.22 | 0.42 | 0.01 | 0.92 | 3.33 | 0.26 |
| N72_DD | −0.32 | 0.50 | 0.57 | −0.22 | 0.42 | −0.01 | −0.76 | 5.05 | 0.52 |
| N72_HH | −0.32 | 0.50 | 0.57 | −0.23 | 0.42 | 0.10 | −0.33 | 4.77 | 0.47 |
| N72_DD_z | −0.32 | 0.50 | 0.57 | −0.23 | 0.42 | 0.09 | −0.38 | 4.31 | 0.54 |

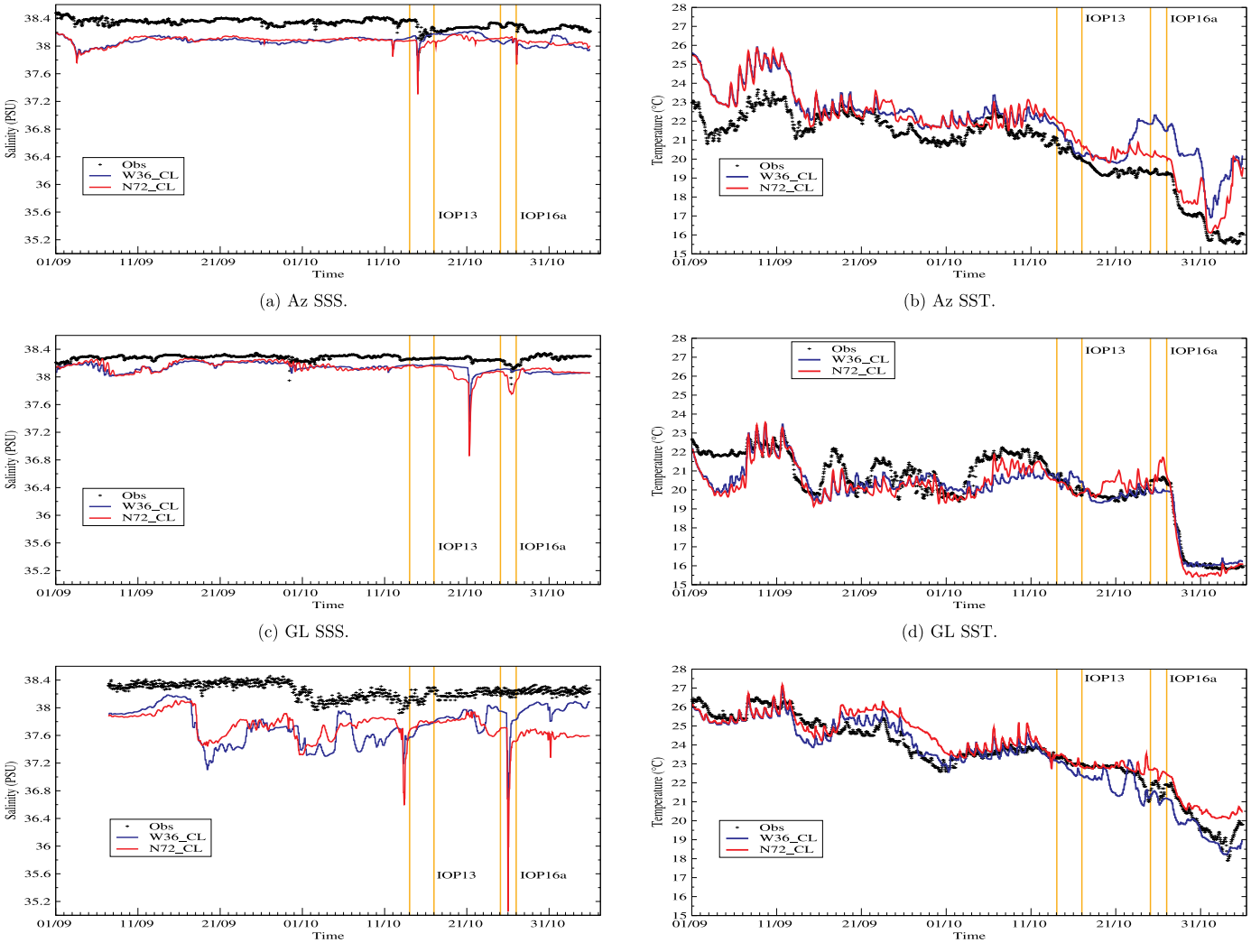


(a) Az SSS. (b) Az SST.

(c) GL SSS. (d) GL SST.

(e) Ta SSS. (f) Ta SST.

**Fig. 3.** Observed and simulated (a,c,e) SSS and (b,d,f) SST time-series during the SOP1 for the (a,b) Azur [Az], (c,d) Lion [GL] and (e,f) Tarragona [Ta] buoys. IOP13 and 16a are underlined in orange. (For interpretation of the references to color in this figure legend, the reader is referred to the web version of this article.)

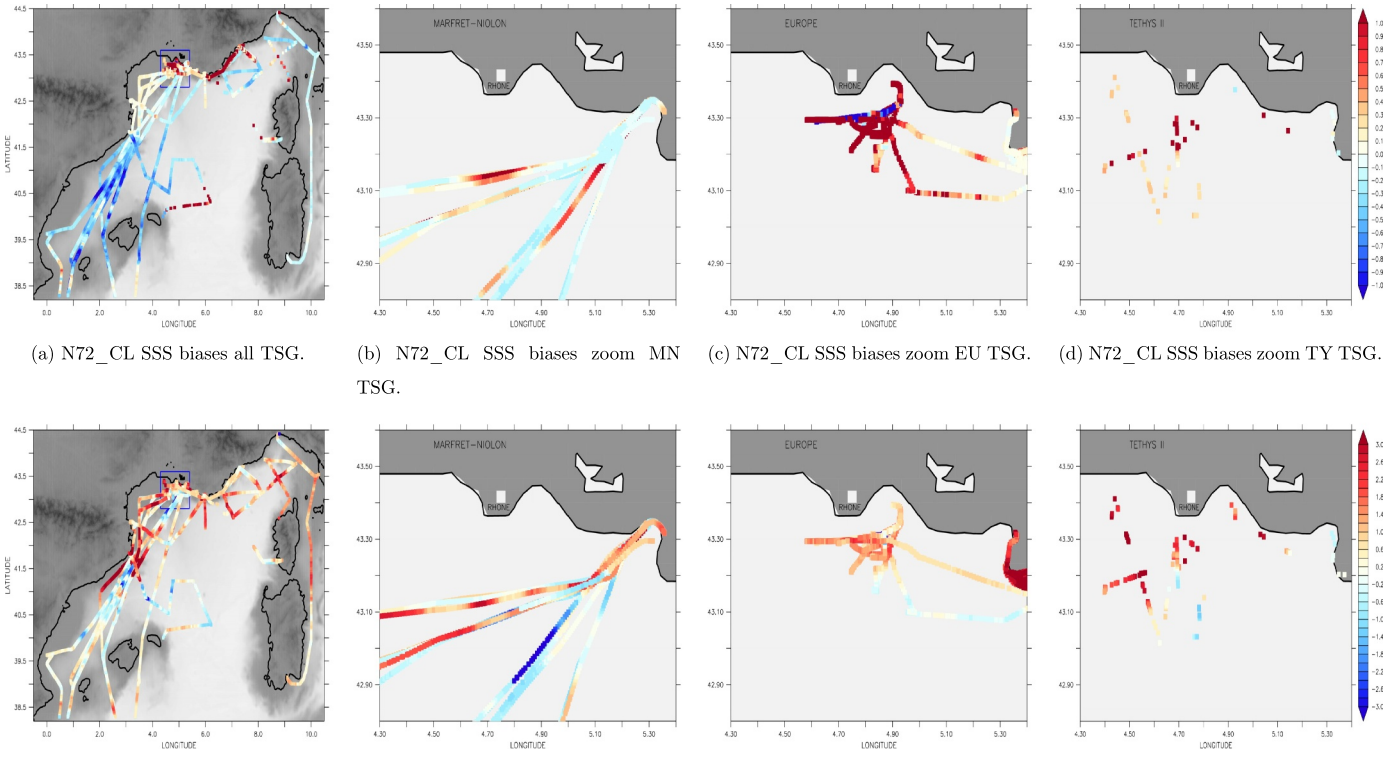


(a) N72_CL SSS biases all TSG. (b) N72_CL SSS biases zoom MN TSG. (c) N72_CL SSS biases zoom EU TSG. (d) N72_CL SSS biases zoom TY TSG.

(e) N72_CL SST biases all TSG. (f) N72_CL SST biases zoom MN TSG. (g) N72_CL SST biases zoom EU TSG. (h) N72_CL SST biases zoom TY TSG.

**Fig. 4.** N72_CL SSS (psu) [upper panels] and SST (°C) [lower panels] bias maps compared to TSG data for all ships tracks over the western Mediterranean (a,e,) and over a zoom near the Rhône river mouth for the MN (b,f), the Eu (c,g) and the TY (d,h) tracks.

observed at the end of the simulation also due to the NC in this place. For the GL buoy, after the 20 October (Fig. 3d), an overestimation is noticed. This is due to the buoy location, south of the NBF, in warmer water. The SSS for all three buoys are not very well reproduced with correlation around 0.2. A quasi-constant underestimation of the SSS is found (Table 3) which is mostly inherited from the initial conditions and a high variability with peaks is simulated (Fig. 3). All of those peaks, present both in W36_CL and N72_CL, are due to precipitation in the atmosphere forcing and each one can be related to different IOPs: IOP13 from the 13 to 16 October with a first phase along the Catalan coast (Fig. 3e) and a second along the French Riviera (Fig. 3a) (Rainaud et al., 2016; Duffourg et al., 2018), IOP15b between the 20 and 22 October impacting the Gulf of Lion (Fig. 3c) (Chazette et al., 2016) and the IOP16a between 24 and 26 October (Duffourg et al., 2016), visible on all three buoys (Fig. 3). Even though the simulated peaks produce too low SSS, most of them are present in the observation. N72_CL and W36_CL differ at the end of the simulation for the Ta buoy where W36_CL has cooler and saltier water than N72_CL (Fig. 3e and f). This is due to the eddy present in the N72_CL which keeps the warmer and less salty water apart from the colder and saltier water offshore. In W36_CL, this eddy is farther from the coast, so the water from the Gulf of Lion reaches the Catalan coast.

Surface in-situ SST and SSS data were collected with thermosalinometers on board of several ships. The Marfet-Niolon freighter (hereafter MN) made weekly round trips between France (Marseille) and Algeria (Mostaganem, Algiers) (Fig. 1a). In the context of the HyMeX program, MN was equipped with a thermosalinometer (TSG) as part of the TRANSMED network (Taupier-Letage et al., 2014). SST was measured with a high-quality sensor SBE38 whereas the surface salinity was obtained with the TSG SBE45 (see TRANSMED Website for more details) along the different routes crossing the western basin shown in Fig. 1a. The TSG data of several others ships, such as the R/V Téthys II (TY), the R/V Europe (Eu) and the container ship Barcelona Express (Ba) (Fig. 1a and b), were collected in the operational Coriolis database and used here to validate the simulations. The comparison to TSG dataset is done using the first model level, knowing that the depth of the TSG measurement could vary (1–3 m) between ships in space and time, and also for a same ship due to its cargo.

The validation against TSG is done in Figs. 4 and 5 showing the biases along ship tracks during the SOP1. The scores are summarized in Tables 3 and 2. The results show that the SSS underestimation concerns the whole domain. For the SST, a positive bias is observed. Yet, a good correlation is obtained for both W36_CL and N72_CL simulations especially for the MN (correlation around 0.9). More locally some areas are subject to a lot of SSS and SST variability like the Catalan coast and river mouths. For example, a zoom on the Rhône River mouth is shown in Figs. 4 and 5 where TSG data are available. In both W36_CL and N72_CL, the SSS is mainly overestimated compared to observations. This can indicate that the influence of the Rhône plume is too small and does not affect enough the SSS at the TSG location (see also Fig. S1 in the supplement). The SST has mainly a positive bias in W36_CL which is reduced in N72_CL. However, bias values vary a lot from one ship to another and can be explained by the date of the sampling which may differ between ships and so as the ocean process sampled.

In order to enlarge the validation, we use satellite observations of SST available during the SOP1 from two different sources. The first satellite SST dataset comes from the Metop-A platform equipped with the Advanced Very High Resolution Radiometer (AVHRR) Pathfinder instrument. The L3P SST product used here is retrieved from the AVHRR infrared channels by using a multispectral technique, applying a re-mapping onto a 0.02°-resolution grid and a cloud mask. It is available twice a day (at midnight and noon). The second satellite SST dataset is obtained using the Spinning Enhanced Visible and InfraRed Imager (SEVIRI) data on the Meteosat Second Generation (MSG) satellite. SST is retrieved from the SEVIRI infrared channels (10.8 and 12.0 μm) using a multispectral algorithm that accounts for regional and

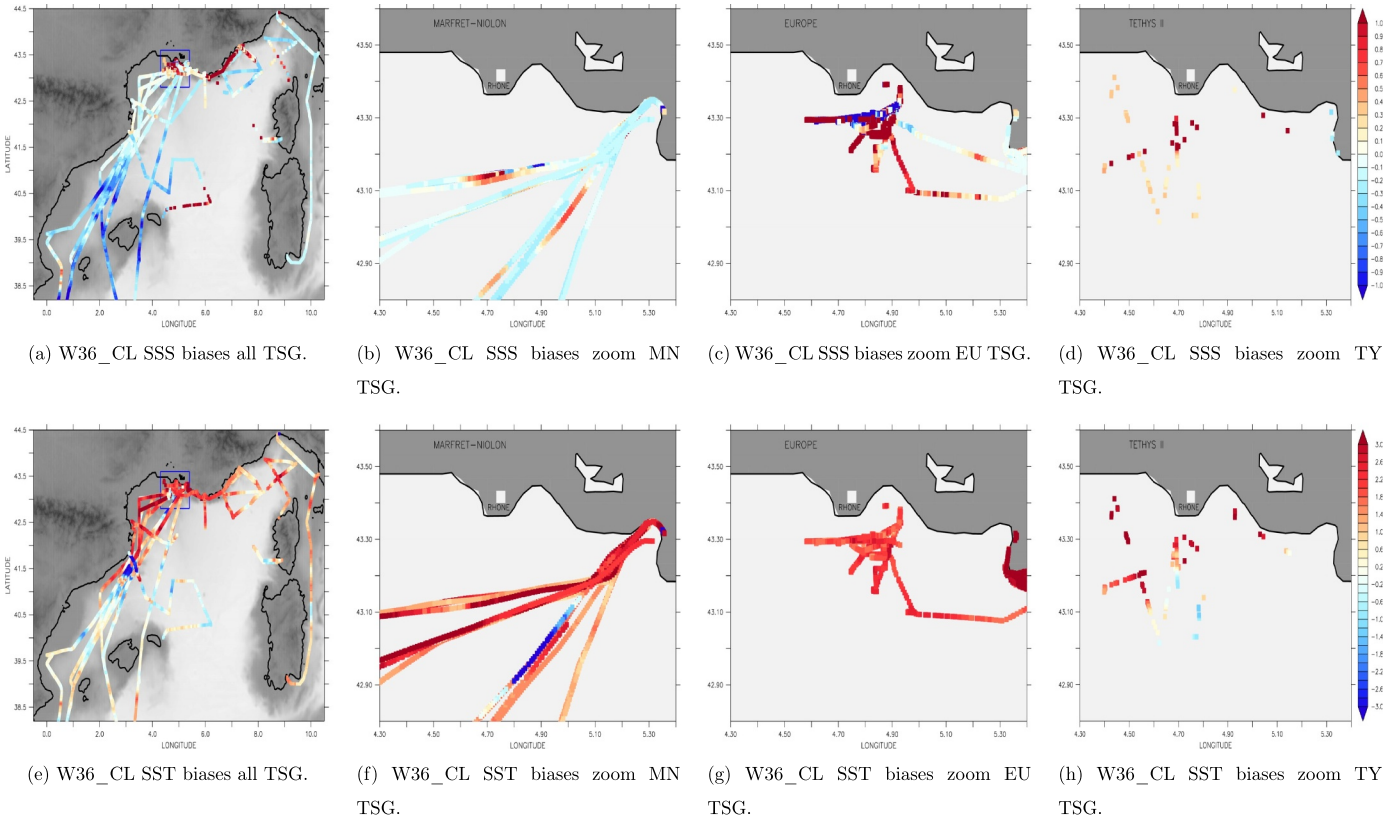


(a) W36_CL SSS biases all TSG. (b) W36_CL SSS biases zoom MN TSG. (c) W36_CL SSS biases zoom EU TSG. (d) W36_CL SSS biases zoom TY TSG.

(e) W36_CL SST biases all TSG. (f) W36_CL SST biases zoom MN TSG. (g) W36_CL SST biases zoom EU TSG. (h) W36_CL SST biases zoom TY TSG.

**Fig. 5.** As Fig. 4 but for W36_CL.

seasonal biases due to changing atmospheric conditions. The L3C product is obtained first by aggregating all 15 min SST data available in one hour time (the priority being given to the value the closest of the nominal time) and then by remapping over a 0.05° regular grid. Both dataset (METOP-L3P and SEVIRI-L3C) were developed by the Group for High Resolution Sea Surface Temperature (GHRSST) and are produced by the European Organization for the Exploitation of Meteorological Satellites (EUMETSAT), Ocean and Sea Ice Satellite Application Facility (OSI SAF) in France. They were made available on the HyMeX database by Centre de Meteorologie Spatiale (CMS) of Météo-France. Their coverages sample the whole WMED domain but depend on the cloud cover. Only satellite SST observations over the North-Western Mediterranean Sea (Fig. 1b) are considered for the validation to be consistent between the two configurations. For each SST satellite dataset, METOP-L3P and SEVIRI-L3C, the mean score for a day is calculated. The evolution of the scores along the SOP1 is shown in Fig. 6. The temporal evolution of the observation availability per day is also displayed on Fig. 6g and h. For METOP-L3P, it shows a good correlation with an average of 0.7 for both W36_CL and N72_CL. Days with weak values of correlation can be related to days with less data, i.e larger cloud covering (Fig. 6g). In average the bias value is around 0.55 °C for W36_CL and it is reduced to 0.37 °C for N72_CL. For SEVIRI-L3C, both simulations show a reduction of the bias (Fig. 6). This is explained by the frequency of observations (every hour) more in agreement with the frequency of the model outputs. In W36_CL, the bias is reduced to 0.3 °C and in N72_CL to 0.2 °C. The correlation is still around 0.7. Comparing with both METOP-L3P and SEVIRI-L3C, a reduction of the bias in N72_CL is found compared to W36_CL. This suggests mainly that the finer horizontal resolution allows a better representation of the SST at fine scale. Furthermore, the improvement in general of the scores in N72_CL might also be affected by the realistic boundary conditions prescribed closer than in W36_CL and impacting directly the area evaluated.

To summarize, the W36_CL and N72_CL simulations give a good representation of the sea surface over the basin. Yet, there is still some issues with some specific areas with larger biases such as close to the river mouths, along the Catalan coast with the effect of the NBF and along the French Riviera impacted by the NC. Moreover, models tend to underestimate the SSS and especially the rapid decreases after HPEs. Several causes can produced the too strong SSS responses to precipitation: errors in precipitations in AROME-WMED in terms of intensity, a more refined vertical grid in N72 and a too small vertical diffusion. This latter aspect has been investigated with an increase of the vertical diffusivity coefficients (Fig. S2 and dummyTXdummy-(Table S2 in the supplement) that does not show significant improvement. The increase in resolution from W36_CL (1/36°) to N72_CL (1/72°) shows some improvements on the SST and the SSS over the basin with bias reduction and slightly higher correlation coefficients.

The validation was also done for the others simulations using daily and hourly runoffs. They do not showed large modification on average over the SOP1 (see Tables 2 and 3 and Figs. S3 to S6 in the supplement) but significant differences are found locally or for short periods of time and this will be discussed on the next section.

It appears that few observations are available close to river mouths, especially when considering the salinity. This makes difficult to clearly evaluate the possible improvements (or degradations) in the ocean simulation when changing the runoff forcing. So, only the sensitivity is considered in the following section.

## 4. River runoff input sensitivity

In this section, the goal is to better understand the impact of several runoff representation on the SSS, SST and local circulation. Only results from the NWMED72 configuration will be described as the validation showed scores improvements with resolution and the experiment with a vertical distribution of runoff was only done with N72_DD_z. Different cases will be studied to focus on the SOP1 flood events.

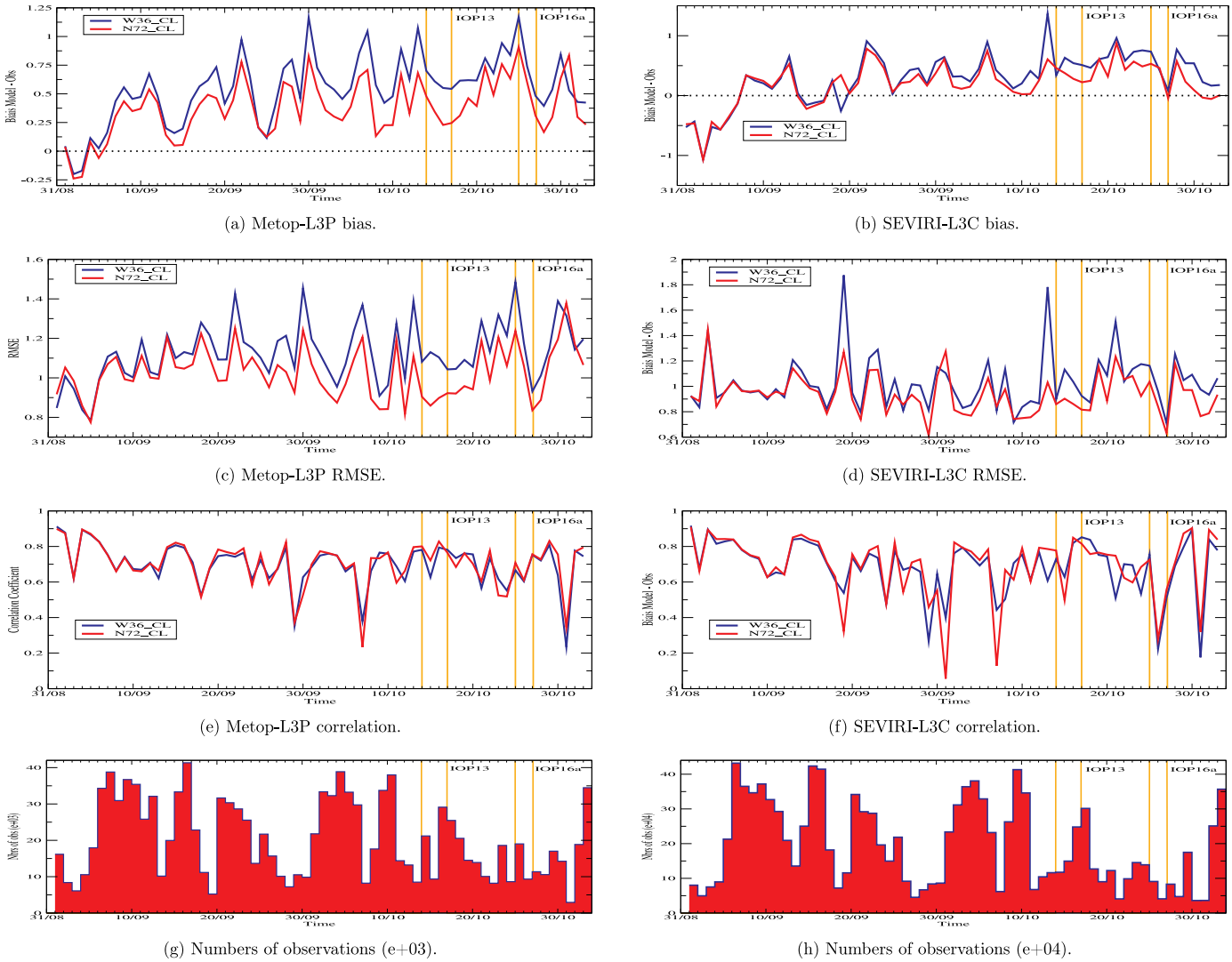


(a) Metop-L3P bias.

(b) SEVIRI-L3C bias.

(c) Metop-L3P RMSE.

(d) SEVIRI-L3C RMSE.

(e) Metop-L3P correlation.

(f) SEVIRI-L3C correlation.

(g) Numbers of observations (e+03).

(h) Numbers of observations (e+04).

**Fig. 6.** Time-series of the simulated SST bias (°C) (a,b), RMSE (°C) (c,d) and correlation coefficient (e,f) against the Metop-L3P (a,c,e) and Seviri-L3D (b,d,f) satellite data in the north–western Mediterranean area. The number of data/pixels available each day is indicated in the lower panels (g,h).

### 4.1. Temporal variation of runoff

#### 4.1.1. Impact on the stratification : The example of the IOP16a

From 25 to 28 October 2012, several MCSs affected the north-western Mediterranean area causing heavy precipitation and flooding in the south-east of France. This event known as the IOP16a is notably described in details in Ducrocq et al. (2014) and Duffourg et al. (2016).

A peak flow was observed in the Côte d'Azur region and Figs. 7a and c show the differences between N72_DD and N72_CL (Fig. 7b and d the difference between N72_DD and N72_HH) of the simulated SSS and SST, for the 27 October in this area. River plumes marked by low SST and SSS are clearly seen along the coast in N72_DD whereas they are absent in N72_CL. Indeed, in N72_DD, the SSS is reduced by more than 1 psu compare to N72_CL (Fig. 7a). Fig. 7e and f show the differences in the Mixed Layer Depth (MLD). The MLD is based on a criterion on density ($\rho_c$ = 0.01 kg.m$^{-3}$) and on the frequency of Brunt–Väisälä, $N$, that characterize the ocean stratification. Therefore, the MLD (h) satisfies the relation $\int_{1m}^{h} N^2 dz \geq g\frac{\rho_c}{\rho_0}$, with $g$ the gravity and $\rho_0$ is the reference density of 1026 kg.m$^{-3}$. In the vicinity of the river mouths, the presence of fresh (very light) water close to the surface increase the stratification of the upper layer and the MLD bounded by this salt barrier is generally small. The larger differences are found between N72_DD and N72_CL and can reach more than 15 m which represent locally a reduction by more than 80% of the N72_CL MLD. The differences between N72_DD and N72_HH are lower in term of MLD but still can represent modifications by 30% to 100%. The thinning of the ocean mixed layer (OML) enhances its sensitivity to the atmospheric forcing. Indeed, the thinner the OML, which is at the interface between the low-atmospheric levels and the ocean thermocline, the more sensitive it becomes to atmospheric forcing. As a consequence of this increase in stratification, the response in SST becomes stronger. Differences in simulated SST close to river mouths can reach 2 °C between N72_DD and N72_CL (Fig. 7c).

Looking more locally on the French Riviera, close to the Argens River, Fig. 8 shows the evolution of the vertical profile of salinity and temperature during 27 October at a point near the river mouth (see the red circle in Fig. 7e). Since the Argens River is not represented in the climatology data set, the ocean profile is well mixed in N72_CL. Indeed, there are no variations in salinity or in temperature nor at the surface nor deeper in the ocean. The hourly observations of the Argens river show that the peak flow occurs early in the morning and then decreased along the day. This decrease is taken into account in N72_HH, whereas in N72_DD the peak flow is smoothed and happens "artificially" in the middle of the day (not shown). In the morning, the stratification is larger in N72_HH with colder and fresher water near the surface. Thus, a maximum difference of about 33 psu and 7 °C at the surface is found

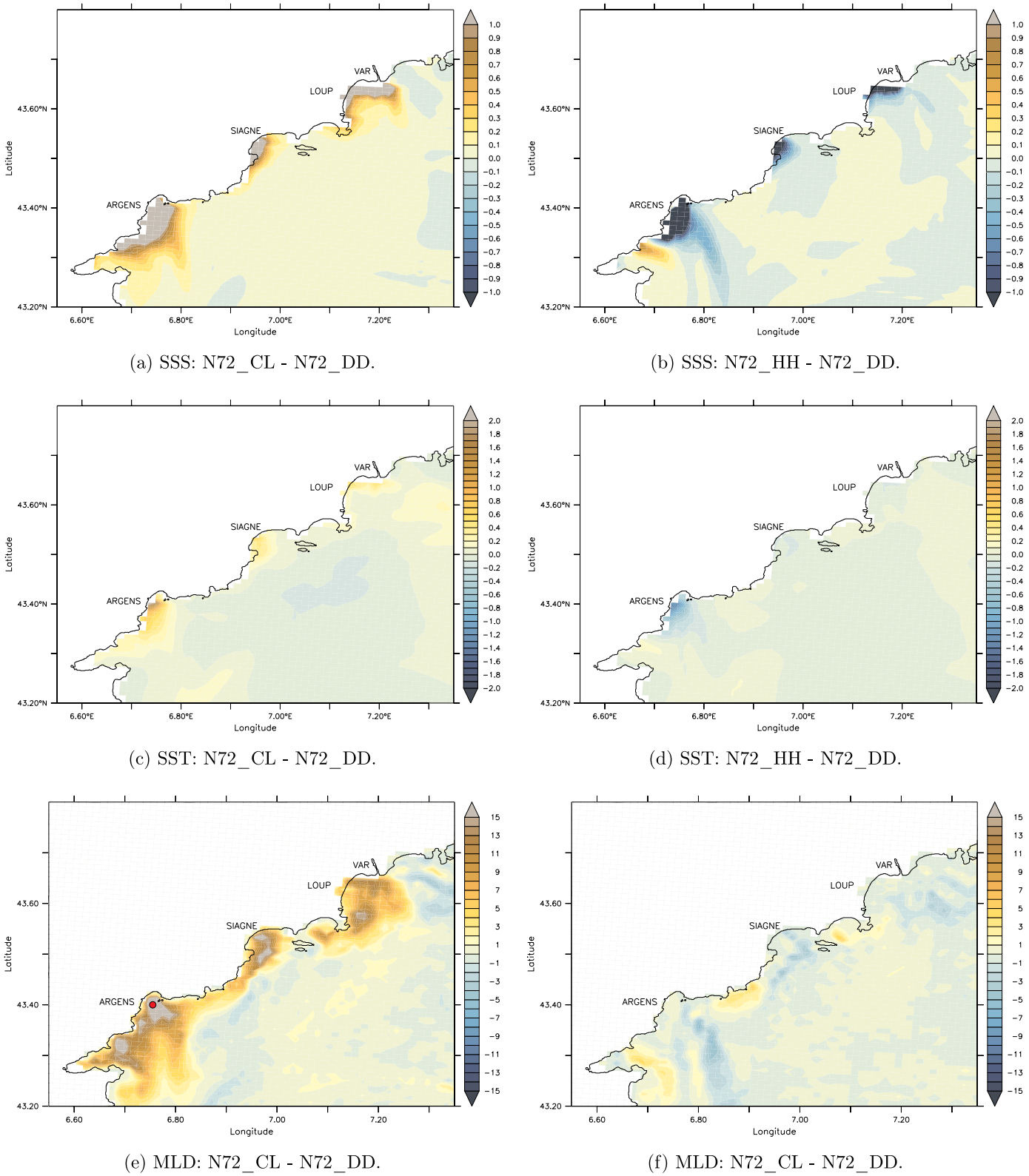


(a) SSS: N72_CL - N72_DD.

(b) SSS: N72_HH - N72_DD.

(c) SST: N72_CL - N72_DD.

(d) SST: N72_HH - N72_DD.

(e) MLD: N72_CL - N72_DD.

(f) MLD: N72_CL - N72_DD.

**Fig. 7.** Differences in the daily mean (a,b) SSS (psu), (c,d) SST (°C) and (e,f) MLD (m) between N72_DD and N72_CL (a,c,e) and between N72_DD and N72_HH (b,d,f) for the 27 October 2012 (IOP16a). Red circle (e) is the location of the vertical profiles shown in Fig. 8. (For interpretation of the references to color in this figure legend, the reader is referred to the web version of this article.)

between N72_HH and N72_CL and of 15 psu and 4 °C between N72_DD and N72_HH. In the afternoon, the stratification in N72_HH is smaller than in N72_DD. During the day the spatial extent of the river plume differs between N72_DD and N72_HH due to the higher frequency in N72_HH. This also explains the differences of SSS and SST, shown in Fig. 7b and d, of, respectively, more than 1 psu and almost 2 °C. The cooling at the end of the day is due to the set up of an upwelling caused by an intense episode of Mistral over the Gulf of Lion which intensifies

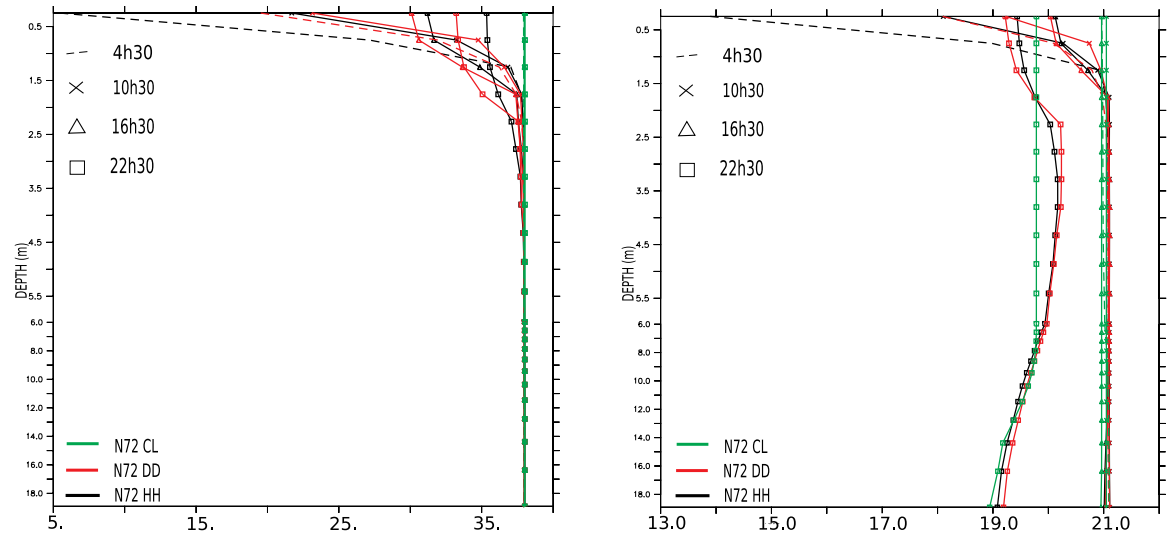


(a) Salinity. (b) Temperature.

**Fig. 8.** (a) Salinity and (b) temperature vertical profiles near the Argens river mouth (see Fig. 7e) during the 27 October 2012 (IOP16a) with a zoom for the 6 m upper layer: N72_CL in green, N72_DD in red and N72_HH in black. (For interpretation of the references to color in this figure legend, the reader is referred to the web version of this article.)

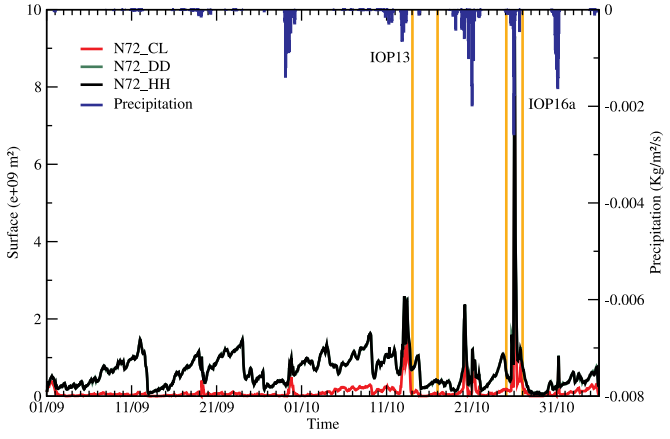


(a) Ebro surface evolution.

**Fig. 9.** Simulated time-serie of the Ebro surface plume ($m^2$) during the SOP1. The upper histogram in blue indicates precipitation rate in $kg/m^2/s$ on average over the area in the AROME atmospheric forcing. (For interpretation of the references to color in this figure legend, the reader is referred to the web version of this article.)

on 28 October (Lebeaupin Brossier et al., 2014; Rainaud et al., 2016; 2017).

*4.1.2. Plume and ocean surface circulation*

The amount of freshwater input from rivers forms a plume in the ocean. Fig. 9 represents the evolution of the Ebro plume surface during the SOP1 for the three NWMED72 simulations. The area is delineated over a domain around the Ebro river mouth with a SSS below 37 psu. On average, the surface of the river plume is 5 times higher in N72_DD than in N72_CL, whereas the plume surface evolution is similar between N72_DD and N72_HH (Fig. 9). This shows that using daily or a hourly frequency do not have a great influence on the extent of the river plume. A high variability is found, even in N72_CL, as large peaks are found related to low-salinity lenses caused by the precipitation that artificially increase the ”plume” surface. Several decreases in the surface are also noticed, mainly in N72_DD and N72_HH, and can be due to various factors such as a decrease in the river flow, a modification of the wind velocity or direction leading to coastward advection or to higher mixing or modification in the circulation in the area.

Another approach is to look at the SSS variability over the SOP1 to estimate the extent of the plume (Fig. 10a). It is shown for a zoom in the Gulf of Lion. The variability is computed as $\sqrt{\frac{\sum_i^N (SSS_i - \overline{SSS})^2}{N}}$ and high values give the influence area of the river plumes. The Rhône river plume appears clearly and have the largest variability. The variability is larger in N72_DD than in N72_CL (Fig. 10b) and river plumes such as for the Aude or the Orb, which are not present in N72_CL, appear along the coast. Here, SSS variability between N72_DD and N72_HH appears quite similar as the differences are very small (Fig. 10c) and confirm previous results on the Ebro case considering plume extent.

Fig. 11a shows SSS and surface current velocity differences between N72_DD and N72_CL over the Gulf of Lion, on the 14 October 2012. This date corresponds to the IOP13 when the Rhône River reached a peak flow (Fig. 2). Most of the differences between simulations are located in the NBF, mainly due to small modifications in the circulation (not shown), and near the Rhône River mouth (Fig. 11a). Fig. 11b displays the surface current direction in the Gulf of Lion for N72_DD and N72_CL and the shade quantify the change in the current direction between the two simulation. Even if the general direction of the current is globally unchanged we can notice some local differences in the Rhône River plume (up to 30°). The largest differences in velocity near river mouths can first be explained by the filtered free surface elevation scheme of Roullet and Madec (2000) that produces a larger additional force in the momentum equation in response to a larger runoff input at the river mouths as found here with the better represented Rhône River flood in N72_DD. In addition, the spreading of freshwater over a heavier fluid results in a decrease in potential energy as it is partially converted into kinetic energy and thus in an intensification of the plume-induced circulation (Chao and Boicourt, 1986). Comparing N72_DD and N72_HH, differences of current intensity are small and do not exceed 0.04 m/s in this area (not shown).

To summarize, changing from climatological runoff forcing to daily forcing has a significant impact on the local ocean surface and stratification. Indeed, during flood events the SSS and SST are lower, when using daily observations, in the vicinity of river mouths. The impact is also observed on the representation of the river plumes becoming larger and thus extend their influence. Furthermore, the current intensity

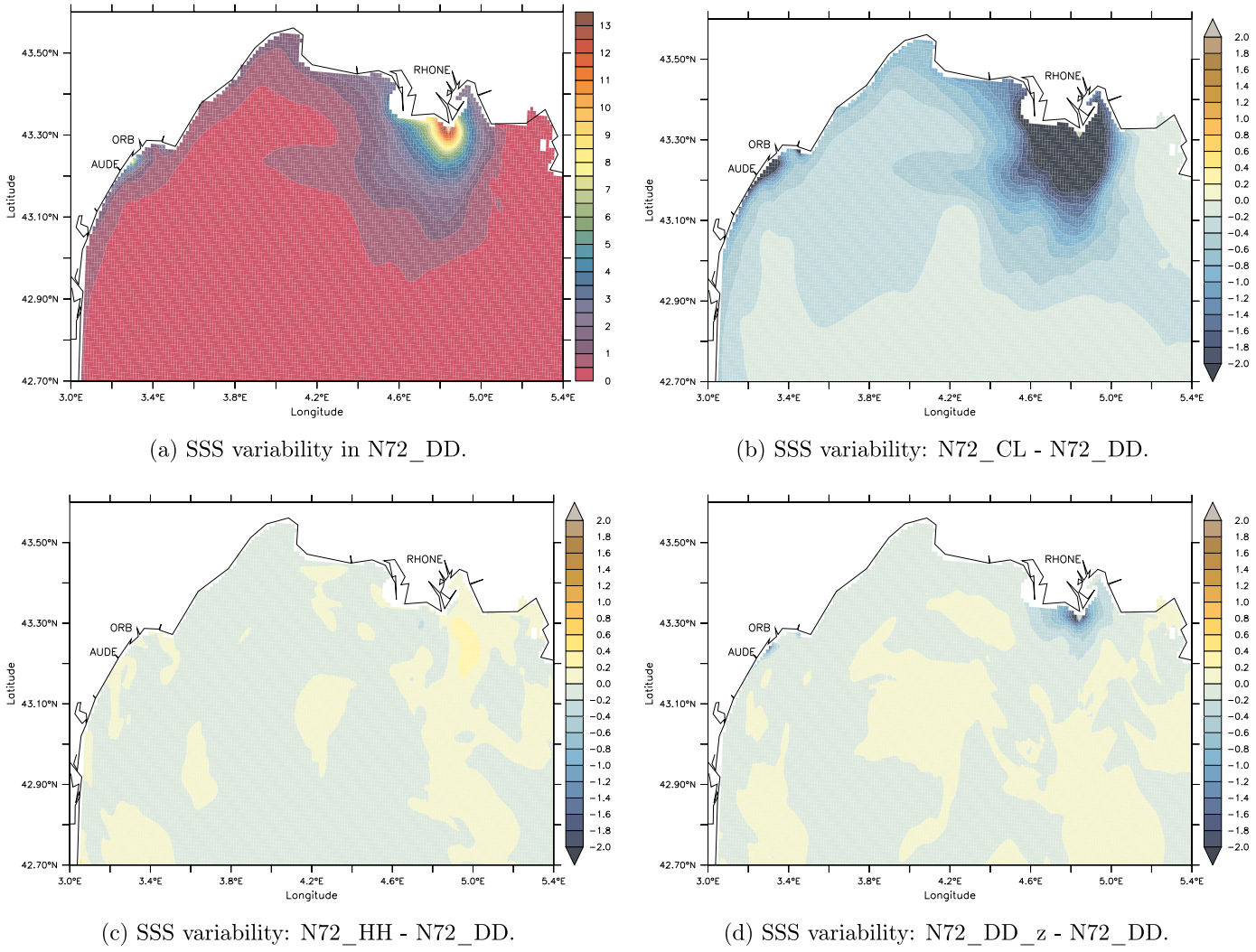


(a) SSS variability in N72_DD. (b) SSS variability: N72_CL - N72_DD.

(c) SSS variability: N72_HH - N72_DD. (d) SSS variability: N72_DD_z - N72_DD.

**Fig. 10.** (a) SSS variability (psu) over the Gulf of Lion during the SOP1 for N72_DD and differences in SSS variability between N72_DD and (b) N72_CL, (c) N72_HH and (d) N72_DD_z.

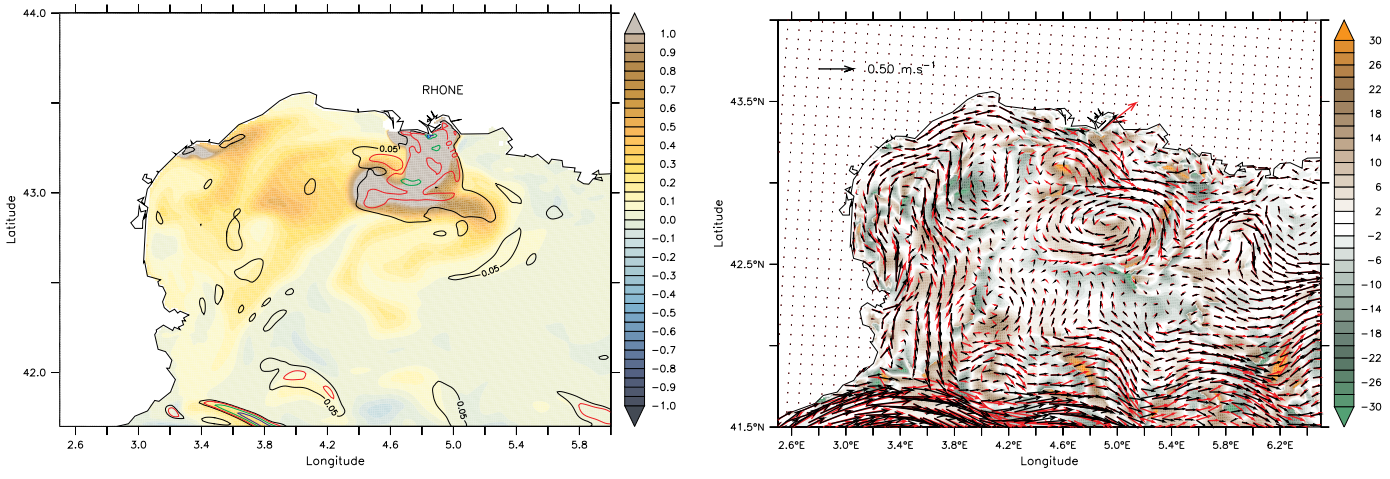


(a) SSS/Surface current: N72_CL - N72_DD. (b) Surface current direction: N72_CL - N72_DD.

**Fig. 11.** Differences between N72_CL and N72_DD over the Gulf of Lion for the 14 October 2012 (IOP13) in (a) SSS (psu) and (b) current direction (° positive clockwise). Colored contours in (a) represent the differences in current velocity (every 0.05 m/s). Black [red] arrows in (b) represent the surface current in N72_CL [N72_DD]. (For interpretation of the references to color in this figure legend, the reader is referred to the web version of this article.)

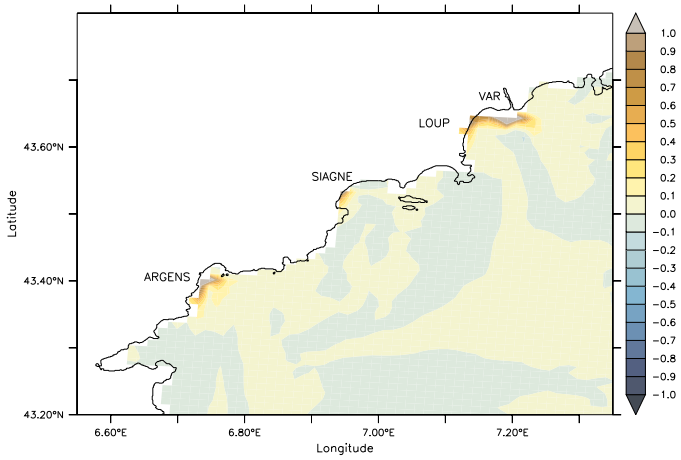


(a) SSS: N72_DD_z - N72_DD.

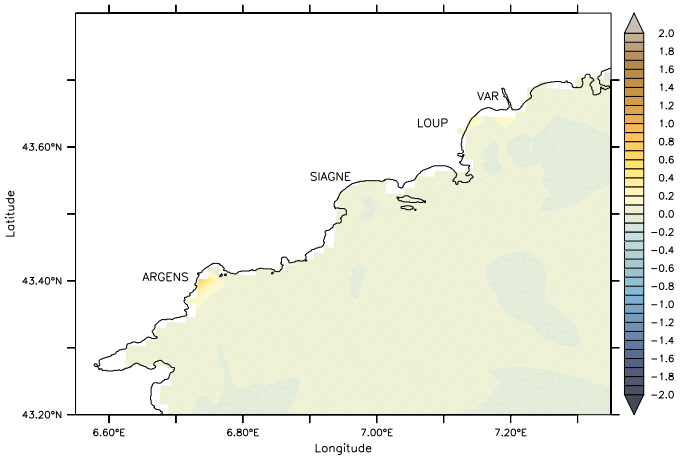


(b) SST: N72_DD_z - N72_DD.

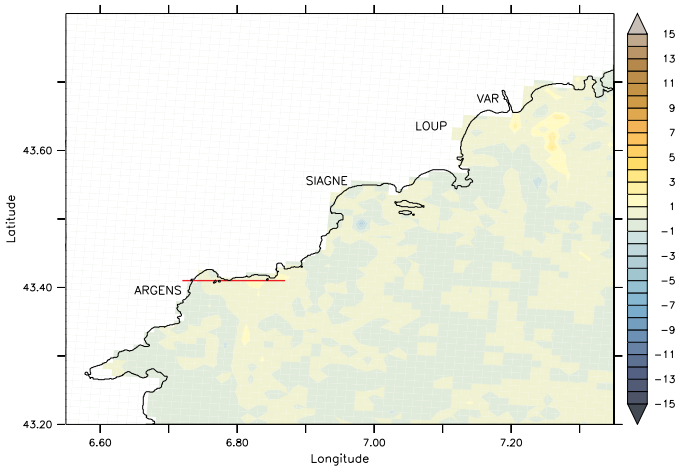


(c) MLD: N72_DD_z - N72_DD.

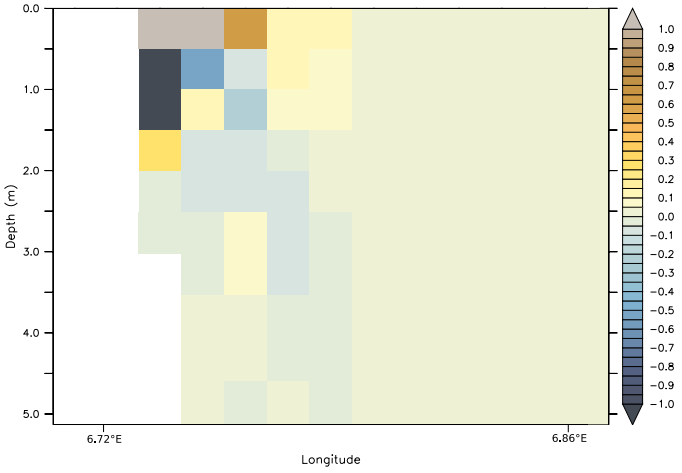


(d) Salinity section: N72_DD_z - N72_DD.

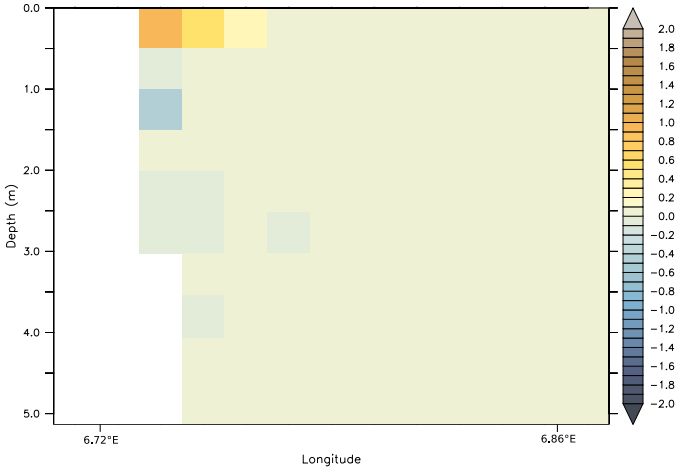


(e) Temperature section: N72_DD_z - N72_DD.

**Fig. 12.** 27 October 2012 (IOP16a): Differences in the daily mean (a) SSS (psu), (b) SST (°C), (c) MLD (m), and for a vertical cross section (shown by the red line in c) in (d) salinity (psu) and (e) temperature (°C). (For interpretation of the references to color in this figure legend, the reader is referred to the web version of this article.)

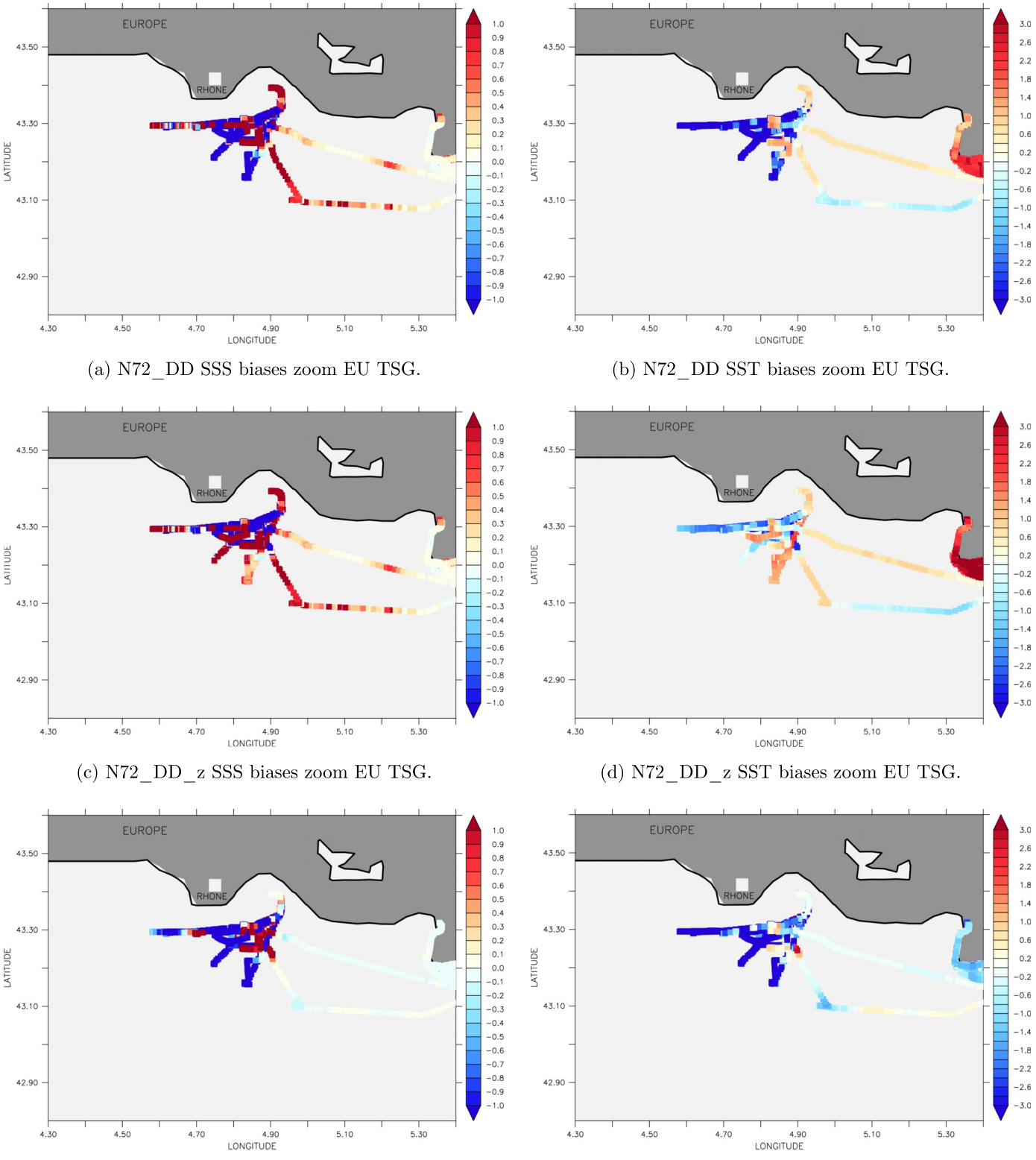


(a) N72_DD SSS biases zoom EU TSG.

(b) N72_DD SST biases zoom EU TSG.

(c) N72_DD_z SSS biases zoom EU TSG.

(d) N72_DD_z SST biases zoom EU TSG.

(e) SSS: N72_DD - N72_DD_z.

(f) SST: N72_DD - N72_DD_z.

**Fig. 13.** (a,c) SSS (psu) and (b,d) SST (°C) bias maps compared to TSG data from the Eu for N72_DD (a,b) and N72_DD_z (c,d). (e,f) differences between N72_DD and N72_DD_z along the Eu TSG track.

within the plumes is increased and the current direction is slightly modified. When changing from daily to hourly runoff forcing, the overall impact is smaller regarding period of time of several months such as the SOP1.

Similar comparisons were done for the WMED36 configuration (not shown) and lead to the same conclusions.

### 4.2. Depth sensitivity

In this section, the impact of a vertical distribution of the runoff

forcing is examined. Indeed, the depth in which the flow is homogeneously distributed can be imposed or calculated inline via a linear expression which is now made available in NEMO v3_6. It takes into account a maximum depth ($depth\_\max$ in meter) and a maximum runoff ($run\_\max$ in kg/m$^2$/s). Therefore, the depth over which the river runoff will be prescribed is calculated as $runoff\_depth = \frac{depth\_\max}{run\_\max} * zrnf$ with $zrnf$ the maximum value of runoff for a specific river over a period of time. In our case, we choose to compute once and for all the depth for each river with $depth\_\max = 7\ m$ corresponding to 14 levels in NWMED72, $run\_\max = 0.6\ kg/m^2/s$ and $zrnf$ the maximum runoff for the considered river over the SOP1. $run\_\max$ is defined just above the maximum value of the Rhône River taken as reference since it represents the biggest river inflow during our period of simulation. Following the same rule, $depth\_\max$ is defined to 7 m compared to the bathymetry depth at the Rhône River mouth.

Fig. 12 shows for 27 October, the surface and vertical sections of the salinity and temperature differences between N72_DD and N72_DD_z near the Argens River whose runoff input is over 1 m depth representing 2 levels in our model. In N72_DD_z, the surface water is warmer and saltier whereas the water "deeper" is colder and less salty than in N72_DD in range of more than 1 psu and 1 °C. The MLD differences over the French Riviera between N72_DD and N72_DD_z are only about few meters (Fig. 12c) but the MLD is increased by 70% at some points near the river mouths in N72_DD_z compared to N72_DD(not shown). The SSS variability differences between N72_DD and N72_DD_z over the whole SOP1 (Fig. 10d) confirm that the major changes are located close to the river mouths.

Like for the others simulations the validation of N72_DD_z was done and scores are shown in Tables 2 and 3. Generally, the scores for moored buoys and TSG in SST and SSS are the same as for N72_DD, or slightly better in some case. TSG biases of N72_DD and N72_DD_z are comparable between the two simulations over the domain.

More locally looking at the Europe ship, SSS (Fig. 13a and c) and SST (Fig. 13b and d) biases showed significant differences. Indeed, Fig. 13e and f represents SSS and SST differences between N72_DD and N72_DD_z. Large variations are only located in the vicinity of the Rhône River mouth and can reach more than 1 psu and 3 °C. Indeed, near the Rhône River mouth in N72_DD the SST is mainly underestimated compared to the observations (Fig. 13b). In N72_DD_z the biases are reduced with an increase of the SST (Fig. 13d). This is due to the vertical redistribution of the input flow that brings less freshwater at the surface but more in the levels below. Indeed, when the river flow is injected in surface, it induces a very thin layer of freshwater and induces a marked salt barrier in the very first meters (1–2 m-depth) of the ocean. This salt barrier thus bounds an internal mixed layer that isolates the layer(s) below from the air-sea interactions. It means that for identical sea surface fluxes, the response of the internal layer will be more intense than for a "typical" mixed layer of 20 to 30 m-depth. When the river flow is injected along a depth, the internal layer is in fact thicker and the salt barrier is less marked. So, due to this (high but) lower stratification in the very upper layer and in case of heat loss, the temperature of the internal layer will decrease less than when runoff forcing is applied in surface [but the cooling will affect a deeper layer (5–7 m-depth)]. The SST decreases but to a lesser extent. And finally, for a same river flow and same atmospheric forcing, it leads to a warmer SST when the flow is vertically distributed. The SSS is also impacted, notably in the influence area of the Rhône plume where the SSS values in N72_DD_z are mostly higher than in N72_DD.

To summarize, the vertical distribution of the runoff is impacting the ocean salinity and temperature near river mouths with saltier and warmer water at the surface than below. The stratification is thus reduced and the MLD is increased.

## 5. Conclusion

Heavy precipitation events occurring in the northwestern Mediterranean basin have a significant impact on the river runoff producing brief and large amount of freshwater running to the sea. Such events constitute major contributions to the water cycle of the region and concern the three Earth compartments: atmosphere, continental surface and ocean.

This study investigates the ocean sensitivity to river forcing. In addition, it allows a first validation of a new ocean configuration over the northwestern Mediterranean basin at 1/72° horizontal resolution. The results of the NEMO ocean model simulations using three types of runoff forcing (monthly climatology, daily and hourly observations) were compared to ocean in-situ observations collected during the SOP1 and satellite data. They showed an agreement with observations on average even if the model tend to underestimate the SSS. Indeed, overestimation of SSS decreases and SST diurnal cycle are noticed. Considering this, our model might overestimate coastal oceanic responses to flood event in the results discussed in this paper. A test with higher vertical diffusivity coefficients for tracers and momentum does not lead to significant improvement. In fact, such oceanic responses strongly depend on the atmospheric flux forcing. Moreover, for N72, our changes in the description of the vertical levels in the ocean might have enhanced the large response of the first layer. So, this problem might be more complex and requires further investigation and notably sensitivity tests on vertical mixing scheme and comparison to what is used for example in operational oceanography for regional models such as at Mercator-Océan. In any case, more salinity observations over the domain and especially near the coast and in the mixed layer would have been useful for validation and in order to better assess the modifications of simulations using runoff observations. To go further in the process of validation, satellite images of chlorophyll could be used to look at the extent and shape of river plumes. However, this implies to correctly relate chlorophyll with modelled tracers. And such evaluation is difficult in the absence of a biogeochemistry compartment in the model.

Then, a detailed comparison between the simulations were done showing large differences on the ocean stratification. During flood events in particular, the SSS is significantly impacted near river mouths. Indeed, observed runoff values allowed to describe the high frequency variability and thus the peak flows. Thus, the extent and variability of river plumes are drastically increased. Large reduction of the MLD is noticed in the vicinity of river mouths in the simulations with observed runoff forcing compared to those using the climatology. This leads to a modification of the SST, as the smaller the MLD is, the higher the response of the ocean mixed layer to the atmospheric forcing is in this area. In future work, the coupled AROME-NEMO system will be used in order to better assess the impact on the air-sea fluxes and on the low-level atmospheric conditions. The current intensity is also increased in the river plume when using runoff observations, in response to the free surface elevation related to the larger amount of incoming freshwater during flood.

Smaller differences are found when comparing simulations using daily and hourly observed forcing. In both cases, the peak flow is well represented but a delay can be artificially introduced in simulations using daily dataset, as in that case the peak flow always happen at noon due to the NEMO time interpolation. This has an impact mostly on the extent of the plume and thus locally on the SSS, SST and MLD.

Finally, a simulation where the runoff is vertically distributed shows local impacts. The salinity and the temperature are changed in surface but also on the ocean levels below. This is due to the lower contribution of freshwater at the surface than deeper. The MLD and the stratification are also changed such as the plume variability near river mouths.

To conclude, the need of using observed runoff data with a high temporal frequency (daily, hourly) to drive ocean models has been illustrated here, especially in case of floods. Indeed, such realistic forcing allows to well reproduce the ocean response to flood event, in term of

stratification and plume dynamics. Nowadays, almost all European ocean forecast centers use monthly mean runoff datasets (Lellouche et al., 2013; Tonani et al., 2014). Therefore the results obtained here show that the use of a higher runoff frequency in forecast system can strongly impact the ocean circulation and stratification in particular in coastal areas. Nevertheless, the use of high frequency river runoff observations requires to collect a large amount of data. Thus, an [and sometimes several] updated and maintained database is [are] needed. In addition, the data collection can be difficult particularly when the studied domain covers several countries. The use of a vertical input for river runoff demands also accurate information about each river depth in the domain and that can be difficult to collect. Nevertheless, the simulation appears to be more realistic.

A way to describe the strong river flow variations properly could be to use river runoff forecasts (at a daily or hourly time step) from a hydrometeorological model and/or a box model approach (Verri et al., 2018). More broadly, this finally calls for the development of integrated prediction systems, that are of strong interest for coastal regions that have a huge vulnerability to severe hazards in many aspects such as urbanization, floods, pollutant, marine ecosystems or erosion.

## Acknowledgments

This work is a contribution to the HyMeX program (*Hydrological cycle in the Mediterranean EXperiment* - http://www.hymex.org) and to the SiMed project (*SImulation of the MEDiterranean Sea*) through INSU-MISTRALS support. The authors acknowledge the Occitanie French region for its contribution to César Sauvage's PhD at CNRM. The authors thank Météo-France for supplying the two moored buoys dataset, in particular the team of the Centre de Météorologie Marine who manages their maintenance, and for supplying the AROME-WMED operational forecasts sponsored by Grants MISTRALS/HyMeX and IODA-MED project (*Innovative Observing and Data Assimilation systems for severe weather events in the MEDiterranean*, ANR-11-BS56-0005). The authors thank Puertos Del Estado for providing data from the Tarragona buoy. The authors also thank Thomas Arsouze (ENSTA/LMD) for his help during the development of the NEMO (v3_6) NWMED72 configuration, and Mercator Océan for supplying the PSY2V4R4 analyses. The authors thank Pere Quintana Seguí from the Observatori de l'Ebre in Barcelona for providing the access to the runoff observations of the Ebro and Jucar Rivers. The authors finally acknowledge the MISTRALS/HyMeX database teams (ESPRI/IPSL and SEDOO/OMP) for their help in accessing to the AROME-WMED forecasts, to the PSY2V4R4 analyses and to the in-situ (moored buoys and TRANSMED thermosalinometer) and satellite (Seviri and Metop) data. The thermosalinograph data from the R/V Téthys II, the R/V Europe and the Barcelona Express were collected and made freely available by the Coriolis project and programmes that contribute to it (http://www.coriolis.eu.org). The TRASNMED system (www.mio.univ-amu.fr/?TRANSMED) was first fostered by the CIESM under the program TRANSMED/PartnerSHIPs (www.ciesm.org/marine/programs/partenerships.htm), and achieved thanks to the support of the INSU MISTRALS/HyMeX program. The MIO has received funding from European FEDER Fund under project 1166-39417.

## Supplementary material

Supplementary material associated with this article can be found, in the online version, at doi:10.1016/j.ocemod.2018.09.005

## References

Barnier, B., Madec, G., Penduff, T., Molines, J.-M., Treguier, A.-M., Le Sommer, J., Beckmann, A., Biastoch, A., Böning, C., Dengg, J., Derval, C., Durand, E., Gulev, S., Remy, E., Talandier, C., Theetten, S., Maltrud, M., McClean, J., De Cuevas, B., 2006. Impact of partial steps and momentum advection schemes in a global ocean circulation model at eddy-permitting resolution. Ocean Dyn. 56 (5), 543–567. https://doi.org/10.1007/s10236-006-0082-1.

Beuvier, J., Béranger, K., Lebeaupin Brossier, C., Somot, S., Sevault, F., Drillet, Y., Bourdallé-Badie, R., Ferry, N., Lyard, F., 2012. Spreading of the Western Mediterranean deep water after winter 2005: time scales and deep cyclone transport. J. Geophys. Res.: Oceans 117 (C7). https://doi.org/10.1029/2011JC007679. C07022

Beuvier, J., Sevault, F., Herrmann, M., Kontoyiannis, H., Ludwig, W., Rixen, M., Stanev, E., Béranger, K., Somot, S., 2010. Modelling the mediterranean sea interannual variability during 1961–2000: focus on the eastern mediterranean transient (EMT). J. Geophys. Res. 115 (C08017). https://doi.org/10.1029/2009JC005950.

Blanke, B., Delecluse, P., 1993. Variability of the tropical Atlantic Ocean simulated by a general circulation model with two different mixed-layer physics. J. Phys. Oceanogr. 23 (7), 1363–1388. https://doi.org/10.1175/1520-0485(1993)023<1363:VOTTAO>2.0.CO;2.

Bormans, M., Garrett, C., Thompson, K., 1986. Seasonal variability of the surface inflow through the strait-of-gibraltar. Oceanol. Acta 9 (4), 403–414.

Brando, V.E., Braga, F., Zaggia, L., Giardino, C., Bresciani, M., Matta, E., Bellafiore, D., Ferrarin, C., Maicu, F., Benetazzo, A., Bonaldo, D., Falcieri, F.M., Coluccelli, A., Russo, A., Carniel, S., 2015. High-resolution satellite turbidity and sea surface temperature observations of river plume interactions during a significant flood event. Ocean Sci. 11 (6), 909–920. https://doi.org/10.5194/os-11-909-2015.

Broche, P., Devenon, J.-L., Forget, P., de Maistre, J.-C., Naudin, J.-J., Cauwet, G., 1998. Experimental study of the Rhone plume. Part I: physics and dynamics. Oceanologica Acta 21 (6), 725–738. https://doi.org/10.1016/S0399-1784(99)80002-4.

Buzzi, A., Tartaglione, N., Malguzzi, P., 1998. Numerical simulations of the 1994 Piedmont flood: role of orography and moist processes. Mon. Weather Rev. 126 (9), 2369–2383. https://doi.org/10.1175/1520-0493(1998)126<2369:NSOTPF>2.0.CO;2.

Chao, S.-Y., Boicourt, W.C., 1986. Onset of estuarine plumes. J. Phys. Oceanogr. 16 (12), 2137–2149. https://doi.org/10.1175/1520-0485(1986)016<2137:OOEP>2.0.CO;2.

Chazette, P., Flamant, C., Raut, J.-C., Totems, J., Shang, X., 2016. Tropical moisture enriched storm tracks over the mediterranean and their link with intense rainfall in the Cevennes-Vivarais area during HyMeX. Q. J. R. Meteorol. Soc. 142, 320–334. https://doi.org/10.1002/qj.2674.

Delrieu, G., Nicol, J., Yates, E., Kirstetter, P.-E., Creutin, J.-D., Anquetin, S., Obled, C., Saulnier, G.-M., Ducrocq, V., Gaume, E., Payrastre, O., Andrieu, H., Ayral, P.-A., Bouvier, C., Neppel, L., Livet, M., Lang, M., du Châtelet, J.P., Walpersdorf, A., Wobrock, W., 2005. The catastrophic flash-flood event of 8–9 september 2002 in the Gard region, France: A first case study for the Cévennes–Vivarais mediterranean hydrometeorological observatory. J. Hydrometeorol. 6 (1), 34–52. https://doi.org/10.1175/JHM-400.1.

Drobinski, P., Ducrocq, V., Alpert, P., Anagnostou, E., Béranger, K., Borga, M., Braud, I., Chanzy, A., Davolio, S., Delrieu, G., Estournel, C., Boubrahmi, N.F., Font, J., Grubišić, V., Gualdi, S., Homar, V., Ivančan-Picek, B., Kottmeier, C., Kotroni, V., Lagouvardos, K., Lionello, P., Llasat, M.C., Ludwig, W., Lutoff, C., Mariotti, A., Richard, E., Romero, R., Rotunno, R., Roussot, O., Ruin, I., Somot, S., Taupier-Letage, I., Tintore, J., Uijlenhoet, R., Wernli, H., 2014. HyMeX: a 10-Year multidisciplinary program on the Mediterranean water cycle. Bull. Am. Meteorol. Soc. 95 (7), 1063–1082. https://doi.org/10.1175/BAMS-D-12-00242.1.

Ducrocq, V., Braud, I., Davolio, S., Ferretti, R., Flamant, C., Jansa, A., Kalthoff, N., Richard, E., Taupier-Letage, I., Ayral, P.-A., Belamari, S., Berne, A., Borga, M., Boudevillain, B., Bock, O., Boichard, J.-L., Bouin, M.-N., Bousquet, O., Bouvier, C., Chiggiato, J., Cimini, D., Corsmeier, U., Coppola, L., Cocquerez, P., Defer, E., Delanoë, J., Girolamo, P.D., Doerenbecher, A., Drobinski, P., Dufournet, Y., Fourrié, N., Gourley, J.J., Labatut, L., Lambert, D., Coz, J.L., Marzano, F.S., Molinié, G., Montani, A., Nord, G., Nuret, M., Ramage, K., Rison, W., Roussot, O., Said, F., Schwarzenboeck, A., Testor, P., Baelen, J.V., Vincendon, B., Aran, M., Tamayo, J., 2014. HyMeX-SOP1: the field campaign dedicated to heavy precipitation and flash flooding in the northwestern Mediterranean. Bull. Am. Meteorol. Soc. 95 (7), 1083–1100. https://doi.org/10.1175/BAMS-D-12-00244.1.

Ducrocq, V., Davolio, S., Ferretti, R., Flamant, C., Santaner, V.H., Kalthoff, N., Richard, E., Wernli, H., 2016. Introduction to the HyMeX Special Issue on 'Advances in understanding and forecasting of heavy precipitation in the Mediterranean through the HyMeX SOP1 field campaign'. Q. J. R. Meteorol. Soc. 142, 1–6. https://doi.org/10.1002/qj.2856.

Duffourg, F., Lee, K.-O., Ducrocq, V., Flamant, C., Chazette, P., Di Girolamo, P., 2018. Role of moisture patterns in the backbuilding formation of HyMeX IOP13 heavy precipitation systems. Q. J. R. Meteorol. Soc. 144 (710), 291–303. https://doi.org/10.1002/qj.3201. QJ-17-0003.R1

Duffourg, F., Nuissier, O., Ducrocq, V., Flamant, C., Chazette, P., Delanoë, J., Doerenbecher, A., Fourrié, N., Di Girolamo, P., Lac, C., Legain, D., Martinet, M., Said, F., Bock, O., 2016. Offshore deep convection initiation and maintenance during the HyMeX IOP 16a heavy precipitation event. Q. J. R. Meteorol. Soc. 142 (S1), 259–274. https://doi.org/10.1002/qj.2725.

Efstathiou, G.A., Lolis, C.J., Zoumakis, N.M., Kassomenos, P., Melas, D., 2014. Characteristics of the atmospheric circulation associated with cold-season heavy rainfall and flooding over a complex terrain region in Greece. Theor. Appl. Climatol. 115, 259–279. https://doi.org/10.1007/s00704-013-0899-8.

Estournel, C., Broche, P., Marsaleix, P., Devenon, J., Auclair, F., Vehil, R., 2001. The Rhone river plume in unsteady conditions : numerical and experimental results. Estuarine, Coastal and Shelf Science 53, 25–38. https://doi.org/10.1006/ecss.2000.0685.

Estournel, C., Kondrachoff, V., Marsaleix, P., Vehil, R., 1997. The plume of the Rhone: numerical simulation and remote sensing. Cont. Shelf Res. 17 (8), 899–924. https://doi.org/10.1016/S0278-4343(96)00064-7.

Fournier, S., Lee, T., Gierach, M.M., 2016. Seasonal and interannual variations of sea surface salinity associated with the Mississippi River plume observed by SMOS and Aquarius. Remote Sens. Environ. 180 (Supplement C), 431–439. https://doi.org/10.1016/j.rse.2016.02.050. Special Issue: ESA's Soil Moisture and Ocean Salinity Mission - Achievements and Applications

Fourrié, N., Bresson, E., Nuret, M., Jany, C., Brousseau, P., Doerenbecher, A., Kreitz, M., Nuissier, O., Sevault, E., Bénichou, H., Amodei, M., Pouponneau, F., 2015. AROME-WMED, a real-time mesoscale model designed for the HyMeX special observation periods. Geosci. Model Dev. 8 (7), 1919–1941. https://doi.org/10.5194/gmd-8-1919-2015.

Herzfeld, M., 2015. Methods for freshwater riverine input into regional ocean models. Ocean Model. 90, 1–15. https://doi.org/10.1016/j.ocemod.2015.04.001.

Houpert, L., Durrieu de Madron, X., Testor, P., Bosse, A., D'Ortenzio, F., Bouin, M.N., Dausse, D., Le Goff, H., Kunesch, S., Labaste, M., Coppola, L., Mortier, L., Raimbault, P., 2016. Observations of open-ocean deep convection in the northwestern mediterranean sea: seasonal and interannual variability of mixing and deep water masses for the 2007–2013 period. J. Geophys. Res.: Oceans 121 (11), 8139–8171. https://doi.org/10.1002/2016JC011857.

Hu, Z.Y., Petrenko, A.A., Doglioli, A.M., Dekeyser, I., 2011. Numerical study of eddy generation in the western part of the Gulf of Lion. J. Geophys. Res.: Oceans 116 (C12). https://doi.org/10.1029/2011JC007074. C12030

Ivančan-Picek, B., Horvath, K., Mahović, N.S., Gajić-Čapka, M., 2014. Forcing mechanisms of a heavy precipitation event in the southeastern Adriatic area. Nat. Hazards 72 (2), 1231–1252. https://doi.org/10.1007/s11069-014-1066-y.

Krichak, S.O., Alpert, P., Dayan, M., 2004. The role of atmospheric processes associated with hurricane Olga in the december 2001 floods in Israel. J. Hydrometeorol. 5 (6), 1259–1270. https://doi.org/10.1175/JHM-399.1.

Lazar, A., Madec, G., Delecluse, P., 1999. The deep interior downwelling, the Veronis effect, and mesoscale tracer transport parameterizations in an OGCM. J. Phys. Oceanogr. 29 (11), 2945–2961. https://doi.org/10.1175/1520-0485(1999)029<2945:TDIDTV>2.0.CO;2.

Lebeaupin Brossier, C., Arsouze, T., Béranger, K., Bouin, M.-N., Bresson, E., Ducrocq, V., Giordani, H., Nuret, M., Rainaud, R., Taupier-Letage, I., 2014. Ocean Mixed Layer responses to intense meteorological events during HyMeX-SOP1 from a high-resolution ocean simulation. Ocean Model. 84, 84–103. https://doi.org/10.1016/j.ocemod.2014.09.009.

Lellouche, J.-M., Le Galloudec, O., Drévillon, M., Régnier, C., Greiner, E., Garric, G., Ferry, N., Desportes, C., Testut, C.-E., Bricaud, C., Bourdallé-Badie, R., Tranchant, B., Benkiran, M., Drillet, Y., Daudin, A., De Nicola, C., 2013. Evaluation of global monitoring and forecasting systems at Mercator Océan. Ocean Sci. 9 (1), 57–81. https://doi.org/10.5194/os-9-57-2013.

Ludwig, W., Dumont, E., Meybeck, M., Heussner, S., 2009. River discharges of water and nutrients to the Mediterranean and Black Sea: Major drivers for ecosystem changes during past and future decades? Prog. Oceanogr. 80 (3–4), 199–217. https://doi.org/10.1016/j.pocean.2009.02.001.

Lyard, F., Lefevre, F., Letellier, T., Francis, O., 2006. Modelling the global ocean tides: modern insights from FES2004. Ocean Dyn. 56 (5), 394–415. https://doi.org/10.1007/s10236-006-0086-x.

Léger, F., Lebeaupin Brossier, C., Giordani, H., Arsouze, T., Beuvier, J., Bouin, M.-N., Bresson, E., Ducrocq, V., Fourrié, N., Nuret, M., 2016. Dense water formation in the north-western Mediterranean area during HyMeX-SOP2 in 1/36° ocean simulations: Sensitivity to initial conditions. J. Geophys. Res.: Oceans 121 (8), 5549–5569. https://doi.org/10.1002/2015JC011542.

Madec, G., NEMO Team, 2016. NEMO ocean engine. Note du Pole de modélisation, Institut Pierre-Simon Laplace (IPSL), France, ISSN No 1288–1619. 27.

Mariotti, A., Struglia, M.V., Zeng, N., Lau, K.-M., 2002. The hydrological cycle in the Mediterranean region and implications for the water budget of the Mediterranean Sea. J. Clim. 15 (13), 1674–1690. https://doi.org/10.1175/1520-0442(2002)015<1674:THCITM>2.0.CO;2.

Marshall, J., Schott, F., 1999. Open-ocean convection: observations, theory, and models. Rev. Geophys. 37 (1), 1–64. https://doi.org/10.1029/98RG02739.

Merheb, M., Moussa, R., Abdallah, C., Colin, F., Perrin, C., Baghdadi, N., 2016. Hydrological response characteristics of Mediterranean catchments at different time scales: a meta-analysis. Hydrol. Sci. J. 61 (14), 2520–2539. https://doi.org/10.1080/02626667.2016.1140174.

Millot, C., 1990. The gulf of Lions' hydrodynamics. Cont. Shelf Res. 10 (9), 885–894. https://doi.org/10.1016/0278-4343(90)90065-T. France-JGOFS, ECOMARGE Particle Fluxes and Ecosystem Response on a Continental Margin

Millot, C., Taupier-Letage, I., 2005. Circulation in the mediterranean sea. Handb. Environ. Chem. Volume 5 (Part K), 29–66. https://doi.org/10.1007/b107143.

Otero, P., Ruiz-Villarreal, M., Peliz, A., 2008. Variability of river plumes off northwest iberia in response to wind events. J. Mar. Syst. 72, 238–255. https://doi.org/10.1016/j.jmarsys.2007.05.016.

Rainaud, R., Lebeaupin Brossier, C., Ducrocq, V., Giordani, H., 2017. High-resolution air–sea coupling impact on two heavy precipitation events in the western mediterranean. Q. J. R. Meteorol. Soc. 143 (707), 2448–2462. https://doi.org/10.1002/qj.3098.

Rainaud, R., Lebeaupin Brossier, C., Ducrocq, V., Giordani, H., Nuret, M., Fourrié, N., Bouin, M.-N., Taupier-Letage, I., Legain, D., 2016. Characterization of air–sea exchanges over the western mediterranean sea during hymex SOP1 using the AROME–WMED model. Q. J. R. Meteorol. Soc. 142, 173–187. https://doi.org/10.1002/qj.2480.

Romero, R., Guijarro, J., Ramis, C., Alonso, S., 1998. A 30-year (1964–1993) daily rainfall data base for the spanish mediterranean regions: first exploratory study. Int. J. Climatol. 18, 541–560.

Roullet, G., Madec, G., 2000. Salt conservation, free surface and varying levels: a new formulation for ocean genereal circulation models. J. Geophys. Res. 105 (C10), 23927–23942. https://doi.org/10.1029/2000JC900089.

Rubio, A., Barnier, B., Jordá, G., Espino, M., Marsaleix, P., 2009. Origin and dynamics of mesoscale eddies in the catalan sea (NW mediterranean): insight from a numerical model study. J. Geophys. Res.: Oceans 114 (C6). https://doi.org/10.1029/2007JC004245. C06009

Schiller, R., Kourafalou, V., 2010. Modeling river plume dynamics with the HYbrid coordinate ocean model. Ocean Model. 33 (1–2), 101–117. https://doi.org/10.1016/j.ocemod.2009.12.005.

Simpson, J., 1997. Physical processes in the ROFI regime. J. Mar. Syst. 12 (1), 3–15. https://doi.org/10.1016/S0924-7963(96)00085-1.

Tarolli, P., Borga, M., Morin, E., Delrieu, G., 2012. Analysis of flash flood regimes in the north-Western and south-Eastern mediterranean regions. Nat. Hazards Earth Syst. Sci. 12, 1255–1265. https://doi.org/10.5194/nhess-12-1255-2012.

Taupier-Letage, I., Bachelier, C., Rougier, G., 2014. Thermosalinometer TRANSMED, Marfret Niolon, Definitive Data Set. Technical Report. SEDOO OMPhttps://doi.org/10.6096/MISTRALS-HyMeX.1127.

Testor, P., Bosse, A., Houpert, L., Margirier, F., Mortier, L., Legoff, H., Dausse, D., Labaste, M., Karstensen, J., Hayes, D., Olita, A., Ribotti, A., Schroeder, K., Chiggiato, J., Onken, R., Heslop, E., Mourre, B., D'ortenzio, F., Mayot, N., Lavigne, H., de Fommervault, O., Coppola, L., Prieur, L., Taillandier, V., Durrieu de Madron, X., Bourrin, F., Many, G., Damien, P., Estournel, C., Marsaleix, P., Taupier-Letage, I., Raimbault, P., Waldman, R., Bouin, M.-N., Giordani, H., Caniaux, G., Somot, S., Ducrocq, V., Conan, P., 2018. Multiscale observations of deep convection in the northwestern Mediterranean Sea during winter 2012–2013 using multiple platforms. J. Geophys. Res.: Oceans 123 (3), 1745–1776.

Tonani, M., Teruzzi, A., Gerasimos, K., Pinardi, N., Crise, A., Adani, M., Oddo, P., Dobricic, S., Fratianni, C., Drudi, M., Salon, S., Grandi, A., Girardi, G., Lyubartsev, V., Marino, S., 2014. The Mediterranean Monitoring and Forecasting Centre, a component of the MyOcean system. Eurogoos Publication.

TRANSMED Website, n.d.http://www.mio.univ-amu.fr/?TRANSMED. [Accessed 3 August 2018].

Tseng, Y.-H., Bryan, F.O., Whitney, M.M., 2016. Impacts of the representation of riverine freshwater input in the community earth system model. Ocean Model. 105, 71–86. https://doi.org/10.1016/j.ocemod.2016.08.002.

Verri, G., Pinardi, N., Frank, B., Tseng, Y.-H., Coppini, G., 2018. A box model to represent estuarine dynamics in mesoscale resolution ocean models. Geophys. Res. Abstr. 20 (EGU2018-15196).

Vörösmarty, C.J., Fekete, B., Tucker, B., 1996. Global River Discharge Database (RivDIS v1.0). Technical Report. UNESCO, Paris.